Preprint typeset using LaTeX style AASTeX6 v. 1.0

arXiv:1607.04325v1 [astro-ph.GA] 14 Jul 2016

A SPECTROSCOPIC STUDY OF BLUE SUPERGIANT STARS IN THE SCULPTOR GALAXY NGC 55: CHEMICAL EVOLUTION AND DISTANCE.

R.P. Kudritzki[1]
Institute for Astronomy, University of Hawaii, 2680 Woodlawn Drive, Honolulu, HI 96822, USA

N. Castro
Department of Astronomy, University of Michigan, 1085 S. University Avenue, Ann Arbor, MI 48109, USA

M. A. Urbaneja
Institut für Astro- und Teilchenphysik, Universität Innsbruck, Technikerstr. 25/8, 6020 Innsbruck, Austria

I.-T. Ho
Institute for Astronomy, University of Hawaii, 2680 Woodlawn Drive, Honolulu, HI 96822, USA

F. Bresolin
Institute for Astronomy, University of Hawaii, 2680 Woodlawn Drive, Honolulu, HI 96822, USA

W. Gieren
Departamento de Astronomía, Universidad de Concepción, Casilla 160-C, Concepción, Chile

G. Pietrzyński[2]
Departamento de Astronomía, Universidad de Concepción, Casilla 160-C, Concepción, Chile

N. Przybilla
Institut für Astro- und Teilchenphysik, Universität Innsbruck, Technikerstr. 25/8, 6020 Innsbruck, Austria

[1]University Observatory Munich, Scheinerstr. 1, D-81679 Munich, Germany
[2]Nicolaus Copernicus Astronomical Center, Polish Academy of Sciences, ul. Bartycka 18, PL-00-716 Warszawa, Poland

ABSTRACT

Low resolution (4.5 to 5 Å) spectra of 58 blue supergiant stars distributed over the disk of the Magellanic spiral galaxy NGC 55 in the Sculptor group are analyzed by means of non-LTE techniques to determine stellar temperatures, gravities and metallicities (from iron peak and α-elements). A metallicity gradient of -0.22 ± 0.06 dex/R_{25} is detected. The central metallicity on a logarithmic scale relative to the Sun is $[Z] = -0.37 \pm 0.03$. A chemical evolution model using the observed distribution of stellar and interstellar medium gas mass column densities reproduces the observed metallicity distribution well and reveals a recent history of strong galactic mass accretion and wind outflows with accretion and mass-loss rates of the order of the star formation rate. There is an indication of spatial inhomogeneity in metallicity. In addition, the relatively high central metallicity of the disk confirms that two extra-planar metal poor HII regions detected in previous work 1.13 to 2.22 kpc above the galactic plane are ionized by massive stars formed in-situ outside the disk. For a subsample of supergiants, for which Hubble Space Telescope photometry is available, the flux-weighted

gravity–luminosity realionship is used to determine a distance modulus of 26.85 ± 0.10 mag.

Keywords: galaxies: distances and redshifts — galaxies: individual (NGC 55) — stars: early type — stars: supergiants

1. INTRODUCTION

The galaxies in the Sculptor group seem to form a filament extended along the line of sight (Jerjen et al. 1998; Karachentsev et al. 2003) with three distinct subgroups, one around the starburst galaxy NGC 253 at about 4 Mpc, the other around NGC 7793 at about the same distance, and the third much closer at half of this distance around NGC 300. While NGC 253, as the largest and most massive galaxy, seems to form the dynamical center of the group, the subgroup around NGC 300 appears to be attracted by the gravitational field of the Local Group.

NGC 55 is member of the nearby subgroup. The near-IR Cepheid study of the Araucaria collaboration places NGC 55 and NGC 300 at roughly the same distance of 1.9 Mpc (Gieren et al. 2005b, 2008). These two galaxies have roughly comparable near-IR magnitudes (K_{tot} = 6.25 and 6.38, respectively, see Jarrett et al. 2003) and mid-IR fluxes ($F_{3.6\mu}$ = 2.02 and 1.63 Jy, $F_{4.5\mu}$ = 1.39 and 1.20 Jy, see Dale et al. 2009) indicating comparable stellar masses. However, while NGC 300 is a regular spiral galaxy of morphological type Scd with a moderate inclination angle (i = 39.9 degrees), NGC 55 is an almost edge-on (i = 78 degrees) barred spiral of type SB(s)m with the bar apparently oriented along the line of sight (de Vaucouleurs 1961; de Vaucouleurs et al. 1991), which closely resembles the Large Magellanic Cloud (Westmeier et al. 2013; Robinson & van Damme 1964).

NGC 300 has been subject to many very detailed studies of its stellar populations, the ISM (atomic and molecular gas distribution, HII regions, planetary nebulae, supernovae remnants, dust content) and the very extended faint stellar disk (see Bresolin et al. 2009, Vlajic et al. 2009, Westmeier et al. 2011, Stasinska et al. 2013, Kang et al. 2016, Toribio San Cipriano et al. 2016, and references therein). In particular, the metallicity of the ISM and the young stellar population has been investigated by detailed quantitative spectroscopic studies of blue supergiant stars (Kudritzki et al. 2008), red supergiants (Gazak et al. 2015), and HII regions (Bresolin et al. 2009). While these three investigations used entirely independent methods for metallicity diagnostics, the results with respect to central metallicity and metallicity gradient agreed extremely well. On the other hand, only a handful of HII regions in the disk of NGC 55 have been studied todate, with an uncertain range in metallicity between [Z] = −0.6 to −0.2[1] (Webster & Smith 1983; Stasinska et al. 1986; Zaritzky et al. 1994; Tüllmann et al. 2003; Castro et al. 2012; Pilyugin et al. 2014). Tüllmann et al. (2003) also investigated two extra-planar HII regions located 0.8 and 1.5 kpc above the disk and found a metallicity almost a factor of ten smaller than solar. Castro et al. (2008) described spectra and spectral morphology of a large sample of hot massive stars, mostly blue supergiants, which were obtained within the Auracaria collaboration (see Gieren et al. 2005a), but so far only a small fraction of these objects, 12 supergiants of early-B spectral type, have been subject to a quantitative spectral analysis (Castro et al. 2012). This work indicated an average metallicity very similar to the LMC, but remained inconclusive about the possibility of a spatial trend in metallicity, in particular a radial metallicity gradient.

NGC 55, a galaxy with significant star formation, is very likely subject to mass accretion and gas outflows (Westmeier et al. 2013; Tüllmann et al. 2003) and, thus, accurate information about metallicity and a potential metallicity gradient might allow to constrain the rates of matter inflow and outflow (see Kudritzki et al. 2015). We have, therefore, resumed the analysis of the spectra obtained by Castro et al. (2008), this time focussing on the supergiants of spectral type B8 to A5, for which the signal-to-noise ratio was sufficient for a quantitative spectral analysis. Because of the many metal lines in their spectra and because of their enormous intrinsic brightness, supergiants of these spectral types are ideal for extragalactic metallicity studies (see Kudritzki et al. 2008, 2012, 2014, and references therein). The selection of targets resulted in a sample of 46 objects distributed over a large range of galactocentric distances. These objects were then analyzed in detail with respect to their effective temperatures, gravities and metallicities and the results are presented in this paper. After a brief description in Section 2 of the observations, the analysis method and the geometrical model used for a de-projection of the location of the targets in the galactic disk, we summarize the results in Section 3. Section 4 focusses on the metallicity and the metallicity gradient and applies a chemical evolution model.

Blue supergiants, as the brightest stars in the Universe at optical wavelengths, are also excellent distance indicators, because their "flux-weighted gravity" $g_F \equiv g/T_{\rm eff}^4$ ($T_{\rm eff}$ in units of 10^4 K) is tightly correlated with their absolute bolometric magnitude, leading to the "Flux-weighted Gravity – Luminosity Relationship (FGLR)" (see Kudritzki et

[1] We transform the nebular oxygen abundances (O/H) to metallicity relative to solar [Z] adopting $12 + \log({\rm O/H})_\odot = 8.69$ from (Asplund et al. 2009)

al. 2003, 2008). Since the distance moduli to NGC 55 obtained with different methods appear to be slightly controversial ranging from 26.4 mag (Cepheids: Gieren et al. 2008) to 26.6 mag (EDD database, http;//edd.ifa.hawaii.edu, see Tully et al. 2009) to 26.8 mag (PLNF: van de Steene et al. 2006), we select a sub-sample of 13 supergiants, for which HST/ACS photometry is available, and determine an independent distance in Section 5 using the most recent calibration of the FGLR method by Urbaneja et al. (2016). Section 6 presents a final discussion.

2. OBSERVATIONAL DATA AND ANALYSIS METHOD

2.1. *Target selection, spectra and photometry*

The spectroscopic observations were carried out in 2004 November 6, 7, 10 using the focal reducer low-dispersion spectrograph FORS2 attached to the ESO VLT-UT2. The Mask eXchange Unit (MXU) mode was used for the multi-object spectroscopy with slit widths of 1 arcsecond in conjunction with the 600B grism providing a nominal resolution of 5 Å in the wavelength range from 3100 to 6210 Å. Four fields (A, B, C, D) with a field of view of 6.8×6.8 arcmin^2 were chosen to cover the whole galaxy, and a total of 200 objects were observed. For the central field C two different mask settings were applied because of the high density of targets in the center of the galaxy. Target selection, field settings and details of the observations, as well as the data reduction, are described in Castro et al. (2008). Their paper provides comprehensive information for all targets. For our work we use coordinates, spectral type, radial velocity, signal-to-noise ratio and the reduced normalized spectra as displayed in the appendix of Castro et al.. We have applied small corrections to some of the Castro et al. radial velocities based on the comparison with our model atmosphere spectra and, therefore, give radial velocity values for all our objects. After careful inspection of the digital spectrum of every target with spectral type B8 to A5 we finally selected 46 objects with spectra suitable for a quantitative spectral analysis. Objects with too strong nebular HII emission contaminating the stellar Balmer lines and with spectra too noisy for the analysis were dropped from the sample in the selection process. The final list is given in Table 1.

Photometry is needed to determine reddening, extinction and apparent bolometric magnitudes which can then be used for a determination of distances through the FGLR method. As pointed out by Castro et al. (2012) the original ground-based photometry obtained with the Warsaw 1.3m telescope at Las Campanas Observatory and provided in the 2008 paper was affected by calibration issues. Re-calibrated photometry, which was used for the early B-supergiant targets in Castro et al. (2012), is available for almost all our targets. However, a comparison with a sub-sample of 13 stars, for which HST/ACS photometry obtained within the ANGST treasury survey of nearby galaxies (Dalcanton et al. 2009) is available, revealed large differences in both the V and I bands of a few tenths of a magnitude. We, thus, decided to only use the sub-sample of 13 stars for the distance determination. The photometry for these objects, together with the information needed for the distance determination, is given given in Table 4.

Castro et al. (2012) have analyzed 12 early B-supergiants of spectral type B0 to B5 and determined effective temperature, gravity and metallicity. In our investigation of the metallicity and the metallicity gradient we include the results from their paper and add the metallicities to enlarge the sample. The list of these objects together with their stellar parameters, galactic positions, galactocentric distances and radial velocities is provided in Table 2. For one of these objects, C1 13, HST photometry is available. It is, therefore, included in the sub-sample used for the distance determination.

2.2. *Geometric and kinematic model of the disk of NGC 55*

The investigation of the metallicity distribution accross the disk of NGC 55 as a function of galactocentric radius requires a de-projection of the targets into the intrinsic plane of the galactic disk in order to calculate galactocentric distances. We use the information given in Table 1 for the de-projection. Our values for the position angle and inclination were guided by the disk model developed by Puche et al. (1991) and are simplified averages of the inner disk. The range of $\pm$ 4 degrees in the inclination angle is used to estimate the uncertainties in deprojected galactocentric distance for the individual objects. We note that Westmeier et al. (2013) have developed an improved model of the warped disk but the changes relative to Puche et al. are relatively small in the inner disk, where our targets are located, and are mostly important in the outer disk, for which Westmeier et al. present new data. De-projected coordinates y perpendicular to the major axis and x along the major axis are given in Table 1 and 2 together with galactocentric distances in units of the isophotal radius R_{25}.

With the de-projected location of our targets we can also compare the radial velocities of our targets. For this purpose we use the kinematic models and rotation curves by Puche et al. (1991) and Westmeier et al. (2013) together with the systemic velocity of Table 1. We note thatWestmeier et al. (2013) have found that the systemic velocity given by Puche et al. (1991) is in error and we use their systemic velocity.

2.3. *Spectral analysis method*

The analysis method is described in detail in Kudritzki et al. (2013, 2014) and in Hosek et al. (2014). In short, we compare normalized observed spectra with synthetic spectra drawn from a comprehensive grid of metal line-blanketed model atmospheres with extensive non-LTE line formation calculations using elaborate atomic models (Przybilla et al. 2006). The grid of models is described in Kudritzki et al. (2008, 2012). The fit procedure uses the higher Balmer lines (usually $H_{5,6,8,9,10}$) in a first step to constrain gravity as a function of effective temperature. This yields a relationship between gravity and effective temperature for each star (see Fig. 3 in Kudritzki et al. 2014). Along this relationship gravity is usually constrained with an accuracy of 0.05 dex.

Then, in a second step, up to 11 spectral windows in the range from 3990 to 6000 Å dominated by metal lines are selected and a comparison between observed and calculated flux is carried out as a function of metallicity for each point along the gravity-temperature relationship (metallicity [Z] is defined as $[Z] = \log Z/Z_\odot$, where $Z_\odot$ is the solar metallicity). In this way, the quality of the metal line fits can be assessed by calculating a χ^2 value for each temperature and metallicity. The minimum of χ^2 and the $\Delta\chi^2$-isocontours around the minimum then yield metallicity and effective temperature of the star with the corresponding fit uncertainties. The final gravity corresponds to the gravity of the gravity-temperature relationship at the temperature determined from the χ^2 minimum. The fit uncertainties of the gravities are a combination of the 0.05 dex accuracy at each temperature as mentioned above and the uncertainty in temperature. The next section will show a few examples of the spectral fits obtained. Note that the χ^2-fit determines stellar metallicity from the contribution of many elements, including the iron peak and α-elements.

In the fit procedure we take into account the fact that the actual spectral resolution can be better than the nominal resolution of the spectrograph in situations of good atmospheric seeing. We, thus, measured the effective resolution for the set of spectra in each field. We found that the spectra of fields A, B, and C are well described with a resolution of 4.5 Å, whereas the resolution obtained for field D is 5 Å. The synthetic spectra were degraded to these resolution values accordingly.

Table 1. NGC 55 late B and early A supergiants

Star	sp. type	$T_{\rm eff}$ K	log g cgs	log g_F cgs	[Z] dex	R/R$_{25}$	x/R$_{25}$	y/R$_{25}$	v$_{rad}$ km/s
(1)	(2)	(3)	(4)	(5)	(6)	(7)	(8)	(9)	(10)
D 29	A3 I	8750^{+150}_{-200}	1.15	$1.38^{+0.09}_{-0.09}$	$-0.50^{+0.10}_{-0.20}$	$0.290^{+0.000}_{-0.000}$	−0.290	$-0.007^{+0.002}_{-0.003}$	98.
D 35	A3 I	8400^{+150}_{-200}	1.00	$1.30^{+0.10}_{-0.12}$	$-0.20^{+0.15}_{-0.10}$	$0.299^{+0.062}_{-0.025}$	−0.237	$-0.182^{+0.045}_{-0.090}$	63.
D 39	A2 I	9900^{+200}_{-250}	1.23	$1.25^{+0.05}_{-0.06}$	$-0.40^{+0.08}_{-0.08}$	$0.200^{+0.009}_{-0.003}$	−0.193	$+0.053^{+0.026}_{-0.013}$	132.
C1 1	A0 I	9450^{+250}_{-250}	1.34	$1.43^{+0.07}_{-0.08}$	$-0.45^{+0.10}_{-0.10}$	$0.200^{+0.038}_{-0.015}$	−0.163	$+0.116^{+0.057}_{-0.029}$	144.
C1 10	A2 I	8700^{+250}_{-250}	1.03	$1.27^{+0.10}_{-0.09}$	$-0.45^{+0.07}_{-0.13}$	$0.171^{+0.073}_{-0.034}$	−0.069	$+0.157^{+0.077}_{-0.039}$	100.
C1 17	A3 I	8500^{+70}_{-70}	1.15	$1.43^{+0.08}_{-0.07}$	$-0.55^{+0.05}_{-0.08}$	$0.258^{+0.127}_{-0.064}$	+0.001	$+0.258^{+0.127}_{-0.063}$	117.
C2 15	A0 I	10500^{+250}_{-200}	1.60	$1.59^{+0.06}_{-0.06}$	$-0.42^{+0.08}_{-0.08}$	$0.194^{+0.094}_{-0.046}$	−0.031	$+0.192^{+0.095}_{-0.047}$	98.
C2 13	A2 I	9000^{+200}_{-200}	1.25	$1.43^{+0.09}_{-0.09}$	$-0.37^{+0.05}_{-0.10}$	$0.096^{+0.034}_{-0.016}$	−0.054	$-0.079^{+0.019}_{-0.039}$	90.
C2 39	A2 I	9000^{+250}_{-100}	1.20	$1.38^{+0.09}_{-0.07}$	$-0.60^{+0.08}_{-0.08}$	$0.143^{+0.034}_{-0.015}$	+0.107	$-0.094^{+0.023}_{-0.047}$	158.
B 7	A0 I	9500^{+100}_{-100}	1.15	$1.24^{+0.06}_{-0.06}$	$-0.40^{+0.05}_{-0.05}$	$0.260^{+0.026}_{-0.010}$	+0.237	$-0.108^{+0.026}_{-0.053}$	162.
A 38	A0 I	9650^{+250}_{-250}	1.33	$1.39^{+0.06}_{-0.07}$	$-0.52^{+0.08}_{-0.08}$	$0.896^{+0.005}_{-0.001}$	+0.893	$-0.081^{+0.020}_{-0.040}$	147.
A 10	A0 I	9550^{+100}_{-100}	1.41	$1.49^{+0.06}_{-0.06}$	$-0.67^{+0.05}_{-0.05}$	$0.735^{+0.093}_{-0.035}$	+0.650	$+0.343^{+0.169}_{-0.084}$	187.
A 43	A2 I	9000^{+250}_{-250}	1.15	$1.33^{+0.09}_{-0.08}$	$-0.60^{+0.10}_{-0.10}$	$0.969^{+0.011}_{-0.004}$	+0.960	$-0.132^{+0.033}_{-0.065}$	185.
A 6	A3 I	8650^{+150}_{-150}	1.18	$1.43^{+0.10}_{-0.10}$	$-0.25^{+0.10}_{-0.10}$	$0.613^{+0.006}_{-0.002}$	+0.608	$-0.079^{+0.019}_{-0.039}$	288.
A 5	A3 I	8750^{+50}_{-50}	1.45	$1.68^{+0.07}_{-0.07}$	$-0.30^{+0.05}_{-0.05}$	$0.600^{+0.004}_{-0.001}$	+0.597	$+0.061^{+0.030}_{-0.015}$	260.
A 28	A2 I	9150^{+150}_{-150}	1.67	$1.83^{+0.09}_{-0.09}$	$-0.30^{+0.13}_{-0.13}$	$0.789^{+0.004}_{-0.002}$	+0.785	$+0.061^{+0.072}_{-0.036}$	219.
A 33	A0 I	9800^{+200}_{-100}	1.86	$1.90^{+0.07}_{-0.06}$	$-0.54^{+0.10}_{-0.10}$	$0.881^{+0.047}_{-0.018}$	+0.840	$+0.265^{+0.131}_{-0.065}$	199.
A 25	B8 I	12200^{+250}_{-250}	1.78	$1.43^{+0.05}_{-0.05}$	$-0.57^{+0.10}_{-0.10}$	$0.923^{+0.171}_{-0.067}$	+0.757	$+0.529^{+0.261}_{-0.130}$	229.
A 14	B9 I	10350^{+150}_{-150}	1.37	$1.31^{+0.05}_{-0.05}$	$-0.45^{+0.10}_{-0.10}$	$0.701^{+0.000}_{-0.001}$	+0.700	$+0.027^{+0.013}_{-0.007}$	225.
A 9	A5 I	7900^{+50}_{-50}	0.85	$1.26^{+0.09}_{-0.09}$	$-0.65^{+0.07}_{-0.07}$	$0.658^{+0.018}_{-0.007}$	+0.643	$-0.141^{+0.035}_{-0.069}$	228.
A 4	A5 I	8200^{+150}_{-150}	1.08	$1.42^{+0.13}_{-0.13}$	$-0.30^{+0.10}_{-0.10}$	$0.586^{+0.001}_{-0.001}$	+0.585	$+0.035^{+0.017}_{-0.009}$	256.
C1 14	A5 I	8200^{+100}_{-100}	0.97	$1.32^{+0.10}_{-0.10}$	$-0.45^{+0.10}_{-0.10}$	$0.187^{+0.090}_{-0.044}$	−0.031	$-0.184^{+0.045}_{-0.045}$	107.
C1 52	A2 I	8400^{+150}_{-150}	0.80	$1.10^{+0.08}_{-0.08}$	$-0.41^{+0.09}_{-0.06}$	$0.263^{+0.000}_{-0.000}$	+0.263	$-0.007^{+0.002}_{-0.004}$	149.
C2 54	B9 I	11000^{+300}_{-300}	1.65	$1.48^{+0.06}_{-0.05}$	$-0.23^{+0.13}_{-0.12}$	$0.275^{+0.014}_{-0.005}$	+0.263	$+0.081^{+0.040}_{-0.020}$	223.
C1 49	A5 I	8150^{+200}_{-200}	0.99	$1.35^{+0.15}_{-0.17}$	$-0.45^{+0.13}_{-0.13}$	$0.242^{+0.001}_{-0.001}$	+0.241	$-0.022^{+0.005}_{-0.011}$	165.
C2 51	B9 I	10600^{+300}_{-300}	1.47	$1.37^{+0.05}_{-0.05}$	$-0.38^{+0.10}_{-0.10}$	$0.237^{+0.003}_{-0.002}$	+0.234	$-0.035^{+0.009}_{-0.017}$	213.
C1 47	A0 I	10250^{+250}_{-250}	1.25	$1.21^{+0.05}_{-0.05}$	$-0.28^{+0.10}_{-0.10}$	$0.232^{+0.004}_{-0.001}$	+0.229	$+0.037^{+0.018}_{-0.009}$	182.
C1 42	A2 I	9450^{+250}_{-250}	1.09	$1.19^{+0.07}_{-0.07}$	$-0.28^{+0.10}_{-0.10}$	$0.208^{+0.015}_{-0.005}$	+0.195	$+0.073^{+0.036}_{-0.018}$	149.
C2 44	A2 I	8850^{+200}_{-150}	1.28	$1.55^{+0.13}_{-0.11}$	$-0.50^{+0.10}_{-0.10}$	$0.382^{+0.163}_{-0.077}$	+0.153	$+0.350^{+0.173}_{-0.086}$	142.
C1 34	B8 I	11500^{+300}_{-300}	1.60	$1.36^{+0.05}_{-0.05}$	$-0.40^{+0.10}_{-0.10}$	$0.116^{+0.005}_{-0.002}$	+0.111	$+0.033^{+0.016}_{-0.008}$	176.
C2 37	A0 I	9750^{+350}_{-350}	1.50	$1.54^{+0.07}_{-0.08}$	$-0.36^{+0.12}_{-0.12}$	$0.092^{+0.001}_{-0.000}$	+0.092	$+0.010^{+0.005}_{-0.002}$	168.
C1 32	B9 I	10200^{+200}_{-200}	1.24	$1.20^{+0.05}_{-0.05}$	$-0.66^{+0.05}_{-0.05}$	$0.501^{+0.240}_{-0.118}$	+0.093	$+0.492^{+0.243}_{-0.121}$	171.
C2 29	B8 I	12500^{+500}_{-300}	1.55	$1.16^{+0.05}_{-0.05}$	$-0.26^{+0.12}_{-0.12}$	$0.038^{+0.005}_{-0.002}$	+0.033	$-0.018^{+0.004}_{-0.009}$	160.
C2 22	A2 I	10500^{+300}_{-500}	1.25	$1.17^{+0.05}_{-0.05}$	$-0.30^{+0.20}_{-0.20}$	$0.175^{+0.085}_{-0.042}$	+0.027	$+0.173^{+0.086}_{-0.043}$	140.
C2 19	A3 I	8750^{+200}_{-200}	1.38	$1.61^{+0.12}_{-0.12}$	$-0.35^{+0.07}_{-0.07}$	$0.067^{+0.033}_{-0.016}$	−0.006	$+0.067^{+0.033}_{-0.016}$	91.
C1 16	A5 I	8200^{+120}_{-120}	1.03	$1.37^{+0.11}_{-0.11}$	$-0.55^{+0.15}_{-0.15}$	$0.328^{+0.162}_{-0.080}$	−0.013	$+0.328^{+0.162}_{-0.081}$	164.
C1 15	B8 I	11200^{+300}_{-300}	1.68	$1.48^{+0.05}_{-0.05}$	$-0.50^{+0.08}_{-0.08}$	$0.287^{+0.141}_{-0.070}$	−0.024	$+0.286^{+0.141}_{-0.070}$	158.
C1 11	A3 I	8625^{+175}_{-175}	1.19	$1.45^{+0.11}_{-0.10}$	$-0.48^{+0.10}_{-0.10}$	$0.132^{+0.053}_{-0.024}$	−0.062	$-0.117^{+0.029}_{-0.058}$	123.
C2 14	B8 I	12000^{+200}_{-200}	1.65	$1.33^{+0.05}_{-0.05}$	$-0.36^{+0.06}_{-0.06}$	$0.379^{+0.185}_{-0.091}$	−0.049	$+0.376^{+0.186}_{-0.092}$	130.

Table 1 continued on next page

Table 1 *(continued)*

Star	sp. type	$T_{\rm eff}$ K	log g cgs	log g_F cgs	[Z] dex	R/R$_{25}$	x/R$_{25}$	y/R$_{25}$	v$_{rad}$ km/s
(1)	(2)	(3)	(4)	(5)	(6)	(7)	(8)	(9)	(10)
C1 8	B8 I	11500^{+200}_{-300}	1.60	$1.36^{+0.05}_{-0.05}$	$-0.51^{+0.08}_{-0.08}$	$0.193^{+0.076}_{-0.035}$	-0.093	$+0.169^{+0.083}_{-0.042}$	149.
C2 8	A0 I	9650^{+150}_{-150}	1.70	$1.76^{+0.06}_{-0.07}$	$-0.66^{+0.05}_{-0.05}$	$0.392^{+0.183}_{-0.089}$	-0.101	$+0.379^{+0.187}_{-0.093}$	95.
D 45	A2 I	9500^{+500}_{-500}	1.58	$1.66^{+0.09}_{-0.13}$	$-0.60^{+0.10}_{-0.10}$	$0.154^{+0.012}_{-0.005}$	-0.142	$+0.058^{+0.029}_{-0.014}$	129.
C2 1	A0 I	9900^{+250}_{-250}	1.58	$1.60^{+0.06}_{-0.07}$	$-0.55^{+0.10}_{-0.10}$	$0.163^{+0.002}_{-0.000}$	-0.162	$-0.023^{+0.006}_{-0.011}$	86.
C2 2	A2 II	8850^{+150}_{-150}	1.71	$1.93^{+0.11}_{-0.11}$	$-0.61^{+0.12}_{-0.12}$	$0.445^{+0.196}_{-0.095}$	-0.155	$+0.417^{+0.206}_{-0.102}$	70.
D 36	B9 I	10850^{+250}_{-250}	1.65	$1.51^{+0.05}_{-0.05}$	$-0.40^{+0.08}_{-0.08}$	$0.313^{+0.083}_{-0.035}$	-0.224	$+0.218^{+0.108}_{-0.054}$	78.
D 6	A3 II	8400^{+150}_{-150}	1.58	$1.88^{+0.13}_{-0.13}$	$-0.60^{+0.15}_{-0.15}$	$0.512^{+0.014}_{-0.005}$	-0.501	$-0.109^{+0.027}_{-0.054}$	58.

NOTE— NGC 55 galaxy parameters: R$_{25}$ = 16.18 arcmin (de Vaucouleurs et al. 1991), position angle PA = 109°(see section 2.2), inclination i =78°± 4°(see section 2.2), central coordinates α_{2000} = $00^{\rm h}$ $14^{\rm m}$ $54.^{\rm s}009$, δ_{2000} = -39°11′49.″267 (Hummel et al. 1986; Puche et al. 1991).
x is coordinate along the major axis, y is the de-projected coordinate along the minor axis.
$g_F = g/T_{\rm eff}^4$ ($T_{\rm eff}$ in units of 10^4 K).

Table 2. NGC 55 late O, early and mid B supergiants

Star	sp. type	$T_{\rm eff}$ K	log g cgs	log g_F cgs	[Z] dex	R/R$_{25}$	x/R$_{25}$	y/R$_{25}$	v$_{rad}$ km/s
(1)	(2)	(3)	(4)	(5)	(6)	(7)	(8)	(9)	(10)
A 08	O9.7 I	27700±1200	2.91	1.14±0.07	−0.37±0.15	$0.634^{+0.003}_{-0.001}$	+0.631	$-0.056^{+0.014}_{-0.028}$	304.
C1 44	B0 I	26200±1500	2.83	1.16±0.07	−0.53±0.15	$0.239^{+0.030}_{-0.012}$	+0.211	$-0.112^{+0.027}_{-0.055}$	181.
C1 9	B1 I	17400±1500	2.37	1.41±0.07	−0.51±0.15	$0.398^{+0.190}_{-0.093}$	−0.081	$+0.390^{+0.192}_{-0.096}$	118.
C1 13	B1 I	24200±1400	2.69	1.15±0.09	−0.45±0.15	$0.207^{+0.099}_{-0.049}$	−0.042	$-0.203^{+0.050}_{-0.100}$	115.
C1 45	B1 I	21500±2500	2.73	1.40±0.12	−0.44±0.15	$0.220^{+0.004}_{-0.001}$	+0.216	$-0.038^{+0.009}_{-0.019}$	179.
A 17	B1 I	22500±2300	2.85	1.44±0.08	-0.45±0.15	$0.738^{+0.006}_{-0.002}$	+0.733	$+0.087^{+0.043}_{-0.021}$	207.
D 27	B2 I	19400±1600	2.41	1.26±0.10	−0.42±0.15	$0.320^{+0.004}_{-0.001}$	−0.317	$+0.045^{+0.022}_{-0.011}$	152.
A 27	B2 I	16300±1100	2.13	1.28±0.09	−0.57±0.15	$0.903^{+0.134}_{-0.052}$	+0.778	$-0.459^{+0.113}_{-0.227}$	199.
C1 53	B2.5 I	18200±2000	2.54	1.50±0.11	−0.21±0.15	$0.292^{+0.026}_{-0.010}$	+0.269	$+0.114^{+0.056}_{-0.028}$	164.
B 31	B2.5 I	16700±900	2.09	1.20±0.08	−0.28±0.15	$0.497^{+0.009}_{-0.003}$	+0.490	$+0.084^{+0.042}_{-0.021}$	190.
A 26	B2.5 I	16100±1000	2.15	1.32±0.09	−0.15±0.15	$0.778^{+0.010}_{-0.004}$	+0.770	$-0.115^{+0.028}_{-0.057}$	220.
A 11	B5 I	14400±1000	1.94	1.31±0.08	−0.37±0.15	$0.691^{+0.034}_{-0.012}$	+0.662	$+0.197^{+0.097}_{-0.048}$	209.

NOTE—Data from Castro et al. (2012).
NGC 55 galaxy parameters: R$_{25}$ = 16.18 arcmin (de Vaucouleurs et al. 1991), position angle PA = 109°(see section 2.2), inclination i =78°± 4°(see section 2.2), central coordinates α_{2000} = 00$^{\rm h}$ 14$^{\rm m}$ 54.$^{\rm s}$009, δ_{2000} = -39°11′49.″267 (Hummel et al. 1986; Puche et al. 1991).
x is coordinate along the major axis, y is the de-projected coordinate along the minor axis.
$g_F = g/T_{\rm eff}^4$ ($T_{\rm eff}$ in units of 10^4 K).

3. RESULTS

The results of the spectral analysis are given in Table 1. Fig. 1 shows a fit of the Balmer lines for two stars taken as examples. As for almost all stars in the sample, H_β is affected by stellar winds and HII region emission. The other Balmer lines, however, allow for an accurate determination of stellar gravities. Fig. 2 displays the isocontours of the χ^2 minimization in the metallicity-temperature plane. We see that while there is some degeneracy between metallicity and temperature, both are well constrained. The $\Delta\chi^2 = 3$ isocontour corresponds to a 1-σ uncertainty, as we have again verified by detailed Monte-Carlo experiments as described by Hosek et al. (2014). This isocontour is used for all stars to determine the errors for temperature and metallicity in Table 1.

Fig. 3 and 4 give an impression of the metal line fits in different spectral windows. Generally, the fits of the spectra are very good and the stellar parameters are well constrained. Most importantly, the accuracy of the metallicities is about 0.1 dex. We note **again** that the metallicity [Z] derived here comes from a fit of metal lines over a wide range of elements, mostly iron, titanium, chromium, magnesium and silicon. In this sense, it represents an average over many elements including the iron group. This is different from HII region metallicities where usually only oxygen is used as a proxy for metallicity. For the comparison of our stellar with HII region metallicities we convert the latter to [Z] = 12 + log(O/H) − 8.69, where 8.69 corresponds to the solar oxygen abundance (Asplund et al. 2009). Such a comparison assumes that the ratios of α-to-iron elements are solar.

3.1. *Evolutionary status*

The evolutionary status of the objects of our full sample can be assessed from Fig. 5, which shows flux-weigthed gravities against effective temperatures compared with stellar evolution calculations. As discussed in detail by Langer & Kudritzki (2014), this "Spectroscopic Hertzsprung-Russell Diagram" is a very useful tool to constrain stellar properties in situations where either the distance is unknown or accurate photometry, which can be used to determine luminosity or bolometric magnitudes, is lacking. From Fig. 5, which compares with the evolutionary tracks by Eckström et al. (2012), it is apparent that the stars of our sample are in an advanced stage of stellar evolution. From their flux weighted gravities we conclude that they represent a mass range from 15 to 40 $M_\odot$. Our sample of selected stars is, thus, comparable to those of our previous studies on other galaxies refererred to in the publications already mentioned. The fact that no lower mass early B-type supergiants are present in our sample is a consequence of the lower V-magnitude limit in the selection of our targets for multi-object spectroscopy. Early B-type supergiants have a much higher bolometric correction than later spectral types. As a consequence, at the same level of V magnitude these objects have higher luminosities and, thus, lower flux-weighted gravities.

3.2. *Metallicity and metallicity gradient*

In Fig. 6 we plot stellar metallicities as a function of galactocentric distance. We see that the two different groups of our sample, early B-type supergiants and late B-type/A-type supergiants give consistent metallicities. This is reassuring, because different types of model atmospheres and atomic models were used for the non-LTE line formation calculations and different methodologies were used for the analysis. We conclude that systematic effects caused by these differences are small.

The average metallicity is somewhat lower than in the LMC and between [Z] = −0.4 to −0.5. A linear regression of the form

$$[Z] = [Z]_0 + grad[Z]\,\frac{R}{R_{25}} \tag{1}$$

accounting for errors in both the x-axis and the y-axis reveals a significant metallicity gradient. We obtain $[Z]_0 = -0.37 \pm 0.03$ dex and grad[Z] $= -0.22 \pm 0.06$ dex/R_{25}. This is the first detection of a metallicity gradient in the disk of this galaxy.

The local scatter around this relation is about 0.15 dex. This is larger than most of the individual metallicity uncertainties and may be indicative of some chemical inhomogeneity in the disk of this galaxy. A few objects above the regression between 0.5 and 0.8 R/R_{25} seem to be outliers. We highlight them with different symbols (stars and squares) in Fig. 6. In order to test whether these outliers are spatially correlated we also plot the de-projected locations of our objects in Fig. 7. We find indeed that these objects cluster on the major axis between 0.5 and 0.8 R/R_{25}.

It is also interesting to check whether some of these chemical abundance outliers are dynamically distinct. For this purpose we use the rotation curve derived by Puche et al. (1991) together with the new corrected systemic velocity of Table 1 to calculate radial velocities of the objects of our sample predicted by the kinematic rotation model. The

comparison with the observed radial velocities measured by Castro et al. (2008) is plotted in Fig. 8. As is evident from the figure, four of the eight suspected chemical outliers are definite kinematical outliers.

The level of chemical enrichment in the disk of NGC 55 obtained from our blue supergiant analysis is generally in agreement with the oxygen abundances of the few HII regions studied. We have used the published line fluxes by Webster & Smith (1983) and applied the "direct method" using the auroral forbidden line [OIII]λ4363. We obtained [Z] = −0.39, −0.34, −0.14, −0.36 for their HII regions 1, 2, 3, 4, respectively. In the same way we find [Z] = −0.52, −0.35, −0.11 for the HII regions 3, 10, "center" investigated by Stasinska et al. (1986). For the central disk HII region in Tüllmann et al. (2003) we obtain [Z] = −0.52.

We note that Pilyugin et al. (2014), applying their newly calibrated strong line method on eight HII regions in NGC 55, four of them in the center, obtain a value of −0.65 below solar and no significant abundance gradient. This is at odds with results obtained by Webster & Smith (1983) and Castro et al. (2012). It is also not supported by our blue supergiant spectroscopy result. Kudritzki et al. (2015) have already pointed to a systematic offset of 0.15 to 0.2 dex between the Pilyugin et al. (2014) HII strong line calibration and their blue supergiant studies of a sample of galaxies. The difference encountered here goes into the same direction, but is slightly larger.

3.3. *Mass-metallicity relationship*

The relationship between the total stellar mass of a galaxy and its average metallicity, the mass-metallicity relationship ("MZR"), is a Rosetta stone to understand the formation and evolution of galaxies. After the pioneering paper by Tremonti et al. (2004), which studied 50,000 SDSS galaxies, revealed the existence of a tight MZR, a large effort has been made to theoretically interpret this relationship either by laborious numerical simulations or by analytical models (see, for instance, Zahid et al. 2014). However, as shown by Kewley & Ellison (2008) the original relationship based on the analysis of strong HII region emission lines is subject to large systematic errors, which are poorly understood. Therefore, Kudritzki et al. (2012) have started to build up a MZR of galaxies in the local Universe, which is based solely on the results of stellar spectroscopy. Our analysis of the young stellar population in the disk of NGC 55 now enables us to add an additional data point to this relationship. This is done in Fig. 9. Note that in order to be consistent with Kudritzki et al. (2012) and Kewley & Ellison (2008) we use the metallicity at two disk scale lengths (corresponding to 0.22 R/R_{25} in the case of NGC 55) for the plot. We have also added the new results by Hosek et al. (2014) and Kudritzki et al. (2014). The stellar mass used for NGC 55 is determined in the next section.

As is evident from Fig. 9 the stellar spectroscopy-based MZR does also form a tight relationship and NGC 55 fits nicely into the middle of it. The SDSS MZR by Andrews & Martini (2013), which is based on stacked spectra of galaxies with similar mass so that the HII region auroral lines can be used for a more precise determination of oxygen abundances, shows a very similar shape. However, there is small shift of 0.15 dex in metallicity or 0.3 dex in stellar mass. In view of the different techniques applied for the diagnostics of metallicities and stellar masses we find the agreement compelling. It seems that many of the strong line calibrations discussed by Kewley & Ellison (2008, see their Fig. 2) can be ruled out.

3.4. *The nature of the extra-planar HII regions in NGC 55*

Tüllmann et al. (2003) have detected two HII regions in the central region of NGC 55 clearly above the plane of the galactic disk at heights of 0.8 and 1.5 kpc based on their adopted distance of 1.6 Mpc. With our new distance of 2.34 Mpc (see Section 5.) the heights above the disk plane increase to 1.13 and 2.22 kpc, respectively. They argue that hydrodynamical considerations rule out an ejection scenario of the ionizing O stars with the surrounding HII region gas from the central disk. As a consequence, the ionizing massive stars must have been born in-situ over the disk. In order to support their argument they determine the metallicity of the two extra-planar HII regions and obtain [Z] = -0.9 ± 0.2, a significantly sub-solar value. They then study one central HII region in the disk and derive [Z] = -0.64 ± 0.1. The abundances are derived using the auroral line [OIII]λ4363 (or an upper limit for the flux in this line) and the R_{23} method in the calibration by McGaugh (1991). From the difference in metallicity they conclude that the extra-planar objects are chemically distinct from the disk population, which supports the idea of in-situ formation over the disk.

However, taking the uncertainties of the metallicties into account one could argue that at the margin of the errors they almost overlap. The chemical proof of in-situ formation all hinges on the metallicity of the one central HII region studied. With our stellar study using a large sample of objects the central metallicity in the disk of NGC 55 is accurately restricted to $[Z]_0 = -0.37 \pm 0.03$ dex. This is a significant difference relative to the metallicity of the two extra-planar HII regions and provides very strong support to the scenario proposed by Tüllmann et al. (2003) of in-situ formation of massive stars above the disk, facilitated by the presence of large amounts of extraplanar gas due

to pronounced mass outflow and inflow in this galaxy (see next Section).

Table 3. Spectral type - $T_{\rm eff}$ relationships of blue supergiant stars

	this work	FP12	K03	EH03	EH03
[Z]	NGC 55	MW	MW	MW	SMC
spectral	$T_{\rm eff}$	$T_{\rm eff}$	$T_{\rm eff}$	$T_{\rm eff}$	$T_{\rm eff}$
type	K	K	K	K	K
(1)	(2)	(3)	(4)	(5)	(6)
B8	11800±490	12200±410	12000	13000	12000
B9	10600±330	10920±220	10500	10750	10500
A0	9800±340	9840±290	9500	9750	9500
A2	9000±330	8960±200	9000	9000	8500
A3	8600±150	8430±60	8500	8500	8000
A5	8130±130			8250	7750

NOTE—FP12: Firnstein & Przybilla (2012); K03: Kudritzki et al. (2003); EH03: Evans & Howarth (2003).

3.5. *Relationship between spectral type and effective temperature*

The set of homogeneous spectra of 46 objects of spectral type B8 to A5 with well determined stellar parameters offers the opportunity to investigate the relationship between spectral type and effective temperature at a metallicity slightly lower than the LMC. For this purpose we use the spectral types assigned by Castro et al. (2008) and the $T_{\rm eff}$ values of our analysis provided in in Table 1. Table 3 gives the mean $T_{\rm eff}$ and standard deviation for each subtype as determined by our spectral analysis. (At spectral type A2 two outliers, D 39 and C2 22, were encountered, which are not included in the calculation of the mean). The comparison with the relationships for the Milky Way obtained by Kudritzki et al. (2003) and more recently by Firnstein & Przybilla (2012) based on the detailed NLTE analysis of high resolution, high S/N spectra shows good agreement. The Evans & Howarth (2003) relationship for the Milky Way is also in agreement, whereas their relationship for the SMC is significantly cooler at later spectral types. We note that Evans & Howarth (2003) have adopted a metallicity [Z] = -0.76 for the SMC, when they calibrated their relationship. This metallicity is significantly lower than for most of our objects studied in NGC 55. In addition, their calibration did not include NLTE effects for the calculation of the metal lines. LTE is very likely sufficient for their SMC objects, because most of them are of luminosity class II. On the other hand, most of the NGC 55 objects have higher luminosities corresponding to luminosity class I and require NLTE calculations to fit the spectrum.

We conclude that at the metallicity level of NGC 55 and for luminosity class I objects we do not see a systematic difference of the spectral type - relationship when compared with the Milky Way.

4. A CHEMICAL EVOLUTION MODEL FOR THE DISK OF NGC 55

The stratification of metallicity of the young stellar population over the disk of a spiral galaxy compared with the radial profiles of ISM gas mass and stellar mass contains crucial information about the chemical evolution history of the galactic disk. In the simple closed box model, which neglects the effects of accretion inflow of material from the cosmic web and of outflow by galactic winds, metallicity at a certain galactocentric radius is uniquley determined by the ratio of the column densities of stellar mass and gas mass at this radius. Metallicity gradients are then a consequence of the variation of this ratio as function of of galactocentric radius. However, it is now well known that accretion and galactic winds play an important role in the chemical evolution of galaxies and, thus, the closed box model can only provide qualitative insight into galaxy evolution. As a simple step further, Kudritzki et al. (2015) have developed a chemical evolution model, in which accretion and outflow are taken into account, but the assumption is made that the rates of mass-gain and mass-loss in units of the star formation rate have been constant. They provide qualitative arguments in their paper in support of this simplifying assumption. Under this assumption, the equations of chemical

evolution can be solved analytically and the observed radial metallicity and mass distributions can then be used to constrain the rates of mass infall Λ and outflow η in units of the star formation rate ψ

$$\eta \equiv \frac{\dot{M}_{loss}}{\psi} \tag{2}$$

and the mass accretion factor

$$\Lambda \equiv \frac{\dot{M}_{accr}}{\psi}. \tag{3}$$

In this way, Kudritzki et al. (2015) have determined mass-loss and accretion rates for 20 nearby disk galaxies. With a well constrained determination of central metallicity and the metallity gradient it is an obvious step to apply the same analysis to NGC 55. This is the first application of this approach on a galaxy with a well determined spatial distribution of metallicity of the young stellar population through spectroscopy. Similar to Kudritzki et al. (2015) we obtain stellar mass column density profiles as a function of galactocentric radius from de-projected mid-IR images at 3.4 μm obtained with the WISE (W1-band) and Spitzer (IRAC) space observatories (for details on the conversion from mid-IR surface photometry to mass-column densities we refer to Kudritzki et al.). The ISM atomic gas mass column density distribution can be obtained from de-projected radio 21 cm observations, where the radio fluxes in the 21 cm line are converted into HI masses and then multiplied by a factor of 1.36 to include the mass of helium and metals. We have re-analyzed the original VLA data cube obtained by Puche et al. (1991) for that purpose. Westmeier et al. (2013) find that the galaxies 21 cm flux is higher than the one obtained by Puche et al. (1991), which is very likely caused by differences in the flux calibration or missing flux through poor coverage of the uv-plane. We apply a factor 1.3 to the Puche et al. data to correct for this effect.

In the inner disks of spiral galaxies the molecular gas can make an important contribution to the total gas mass. An estimate of the molecular gas mass is usually obtained from an observation of CO which is then converted to molecular hydrogen mass, for which the factor 1.36 is then applied again to include helium and metals. Unfortunately, in the case of NGC 55 no CO observations are available. We, therefore, use an indirect way to estimate the column density distribution of the molecular mass. We start from the de-projected observation of the 21 cm continuum radio flux, which is then converted into far-IR flux using the FIR-radio flux correlation and yielding the radial profile of star formation rate (see Ho et al. 2010). The star formation rates are then transformed into molecular hydrogen column densities by application of the molecular Kennicutt-Schmidt law as parameterized by Leroy et al. (2013).

The integrated total stellar mass of the disk of NGC 55 (in units of the solar mass) is log $M_{star} = 9.29$. We note that the mass depends on the distance assumed. We have used a distance of 2.34 Mpc, which we derive in the following section.

Fig. 10 displays the column densities of stellar and ISM atomic and molecular masses obtained in this way as a function of galactocentric radius. Obviously, the molecular gas contribution is only important in the central disk region and has only a weak effect on the constraints for outflow and accretion. The central stellar mass profile does not show a significant indication of a bulge contribution. We, thus, refrain from an attempt of bulge de-composition as carried out for most of the galaxies in Kudritzki et al.

Applying the same fit algorithm of the observed metallicity distribution as Kudritzki et al. we can then constrain the rate of outflow and accretion. We obtain $\eta = 0.72$ and $\Lambda = 1.38$. This means that the chemical evolution of NGC 55 is characterized by large amounts of gas outflow and infall. Compared to all the other galaxies studied by Kudritzki et al. the infall rate of NGC 55 is by far the largest. Qualitatively, this agrees well with the detailed morphological, kinematic and dynamic study by Westmeier et al. (2013) and their conclusion that "internal and external processes, such as satellite accretion or gas outflows, have stirred up the gas disc".

With the large value of Λ detected it is interesting to investigate in which way NGC 55 is different from the other galaxies analyzed with the same chemical evolution approach. We compare with the sample of galaxies with well determined η and Λ in Kudritzki et al. (see their Figure 11) and find the striking anti-correlation of Λ with total galaxy stellar mass shown in Fig. 11. From all the spiral galaxies studied so far with our method NGC 55 has by far the lowest mass and it seems that Λ increases significantly with decreasing mass. A power law $\Lambda \sim M_{star}^{-\alpha}$ with $\alpha = 0.8$ provides a reasonable fit to the data, except at the high mass end, where very small values of Λ are observed. We note that on the "main sequence of galaxies" star formation increases with stellar mass following a power law $\psi \sim M_{star}^{\beta}$ with β between 0.7 to 1.0 (see Lee et al. 2015 and references therein). Consequently, for the sample displayed in Fig. 11 the mass accretion rate $\dot{M}_{accr}$ can be expressed as $\dot{M}_{accr} \sim M_{star}^{-\alpha+\beta}$. This means that the mass accretion rates depend only very weakly on galaxy mass, because α and β almost cancel each other in the exponent. (At high galaxy masses

accretion is probably reduced by shocks formed by the accretion process, which heat the infalling material and slow down accretion onto the disks).

To confirm this scenario is beyond the scope of this paper. We will need more studies in particular at the low mass end of the observed relation. This will require more detailed spatially resolved observations of the atomic and molecular gas in addition to multi-object stellar or HII-region spectroscopy and a careful investigations of star formation rates. The corresponding work is presently under way.

Fig. 6 shows the metallicity distribution calculated with our best fit chemical evolution model compared to the observed metallicities. The model provides a good fit to the observed data. We take this as a confirmation that the concept to retrieve important information on galaxy evolution from the spatial distribution of the metallicity of the young stellar population or the ISM is a promising approach with large potential.

Table 4. NGC 55 supergiants with HST photometry used for FGLR

Star	log g_F	m_{bol}	V	I	E(B-V)	BC	$(V-I)_0$
	cgs	mag	mag	mag	mag	mag	mag
(1)	(2)	(3)	(4)	(5)	(6)	(7)	(8)
C1 17	$1.43^{+0.08}_{-0.07}$	18.905±0.038	19.295±0.002	19.072±0.003	0.109±0.010	-0.041±0.020	+0.083±0.012
C2 15	$1.59^{+0.06}_{-0.06}$	19.024±0.048	19.709±0.003	19.546±0.003	0.116±0.006	-0.314±0.044	+0.014±0.006
C2 13	$1.43^{+0.09}_{-0.09}$	18.768±0.059	19.085±0.002	18.936±0.002	0.061±0.011	-0.123±0.046	+0.071±0.014
C1 14	$1.32^{+0.10}_{-0.10}$	18.551±0.068	18.790±0.002	18.584±0.002	0.077±0.018	+0.008±0.037	+0.107±0.008
C1 34	$1.36^{+0.05}_{-0.05}$	18.155±0.065	19.484±0.003	19.204±0.003	0.229±0.007	-0.598±0.062	-0.013±0.008
C2 37	$1.54^{+0.07}_{-0.08}$	18.864±0.075	19.534±0.003	19.338±0.003	0.129±0.009	-0.256±0.069	+0.030±0.010
C2 29	$1.16^{+0.05}_{-0.05}$	17.417±0.100	19.239±0.002	18.863±0.003	0.314±0.012	-0.819±0.092	-0.026±0.015
C2 22[a]	$1.17^{+0.05}_{-0.05}$	17.394±0.107	18.737±0.002	18.336±0.002	0.277±0.015	-0.456±0.096	+0.046±0.019
C2 19	$1.61^{+0.12}_{-0.12}$	19.532±0.061	19.532±0.003	19.729±0.003	0.099±0.014	-0.064±0.042	+0.056±0.017
C1 16	$1.37^{+0.11}_{-0.11}$	18.872±0.051	19.281±0.002	19.025±0.002	0.131±0.011	+0.010±0.037	+0.088±0.014
C1 11[a]	$1.45^{+0.11}_{-0.10}$	19.418±0.058	19.848±0.003	19.621±0.003	0.116±0.012	-0.058±0.042	+0.078±0.015
C2 14	$1.33^{+0.05}_{-0.05}$	18.554±0.047	19.328±0.002	19.321±0.003	0.027±0.005	-0.689±0.044	-0.027±0.005
C1 13	$1.15^{+0.09}_{-0.09}$	16.328±0.133	19.378±0.003	19.301±0.003	0.211±0.008	-2.375±0.130	-0.303±0.014

NOTE—Bolometric correction BC and intrinsic color $(V-I)_0$ calculated from model atmospheres (see Kudritzki et al. 2008 for details).

[a]Not included in distance determination because of variability (see text).

5. DISTANCE

The sub-sample of objects in Table 4 with HST/ACS photometry can be used to determine a distance using the FGLR technique briefly described in section 1. With temperature, gravity and metallicity determined by spectroscopy we can calculate the intrinsic spectral energy distribution of our targets and their $V-I$ colors. Comparison with the observed colors then yields the reddening $E(B-V)$ [we apply the relation $E(B-V) = 0.78\,E(V-I)$] and, by assuming $R_V = A_V/E(B-V) = 3.2$, the value of extinction A_V. Adding the bolometric correction calculated from the intrinsic energy distribution to the de-reddened V-magnitude we then obtain de-reddened apparent bolometric magnitudes for each object. The values obtained for the reddening, the bolometric corrections and the bolometric magnitudes are also given in Table 4, together with the logarithm of the flux-weighted gravities.

The NGC 55 Cepheid search carried out by Pietrzyński et al. (2006) in V and I provided us with repeated photometry of the targets in Table 4 over a period of 900 days, allowing us to assess their photometric variability. According to Bresolin et al. (2004) blue supergiants usually show only a small amount of photometric variability, which does not significantly affect distances determinations through the FGLR method. But in a few cases larger photometric variations are encountered. Of the objects in Table 4, star C2 22 showed clear signs of variability, increasing in brightness in both V and I by 0.2 mag over the observed period. It was, therefore, not included in the final sample used for the distance determination. In addition, C1 11 showed brightness variations up to 0.1 mag and was also dropped from the sample. For all other objects the level of variability inferred from correlated changes in V and I is smaller than or equal to 0.05 mag. For those objects we add an additional uncertainty of 0.05 mag to the bolometric magnitude uncertainties in Table 4 to account for blue supergiant variability in the distance determination described below.

Fig. 12 demonstrates that the bolometric magnitudes and flux-weighted gravities of our objects are tightly correlated. This is the "Flux-weighted Gravity – Luminosity Relationship (FGLR)" introduced in section 1. As in previous work (Kudritzki et al. 2012, 2014; Hosek et al. 2014; U et al. 2009; Urbaneja et al. 2008) it can be used to determine extragalactic distances. Most recently, Urbaneja et al. (2016) have introduced a new calibration of the FGLR through

a spectroscopic study of 90 blue supergiants in the LMC. Based on the analysis of the (M_{bol}, log g_F) diagram of their 90 LMC supergiants they find that the FGLR changes its slope at log $g_F = 1.29$. They fit a 2-component FGLR with two slopes to their data and determine a new zero point. The new FGLR in absolute bolometric magnitude M_{bol} is given by

$$\log g_F \geq \log g_F^{\rm break} : M_{\rm bol} = a(\log g_F - 1.5) + b \quad (4)$$

and

$$\log g_F \leq \log g_F^{\rm break} : M_{\rm bol} = a_{\rm low}(\log g_F - \log g_F^{\rm break}) + b_{\rm break} \quad (5)$$

with

$$b_{\rm break} = a(\log g_F^{\rm break} - 1.5) + b. \quad (6)$$

with $\log g_F^{\rm break} = 1.29$, $a = 3.46 \pm 0.12$, $b = -7.92 \pm 0.03$ mag and $a_{\rm low} = 7.93 \pm 0.25$.

To determine the distance to NGC 55 we use the observed flux-weighted gravities to calculate absolute magnitudes by means of the calibration FGLR. We than calculate individual distance moduli for each object and obtain the final distance from a weighted mean which accounts for the observational errors in bolometric magnitude and the logarithm of flux-weighted gravity. We obtain a distance modulus of $m - M = 26.85 \pm 0.08(r) \pm 0.05(s)$. The systematic error comes from uncertainties of the FGLR parameters. Fig. 12 also shows the calibration FGLR shifted to the distance determined.

We realize that our FGLR-based distance modulus is 0.42 mag larger than the $m - M = 26.43 \pm 0.09$ obtained by Gieren et al. (2008) in our Araucaria collaboration. Gieren et al. use ground based J- and K-band photometry of Cepheids in conjunction with the V and I photometry by Pietrzyński et al. (2006). This is a very reliable technique, in particular, because of the use of K-band, which minimizes the effects of reddening for the Cepheids (we note that the average reddening of the targets in Table 4 is $E(B-V) \approx 0.15$ mag, very similar to the reddening found in the Cepheid study). Usually the agreement between Cepheid and FGLR distances is satisfactory. For instance, in the case of the Sculptor group neighbor galaxy NGC 300 our new FGLR calibration yields a distance modulus of $m - M =$ **26.33**, while Gieren et al. (2005b) obtain 26.37 again from ground-based photometry combining the V, I, J and K bands. As mentioned in the Section 1., the physical parameters of the two galaxies are very similar. However, there is one fundamental difference between NGC 300 and NGC 55, namely the fact that the latter is almost an edge on galaxy. As the result, the surface brightness of NGC 55, for instance in the K-band, is significantly brighter than for NGC 300 (see Fig. 13). This increases the potential of blending with nearby fainter objects, which would increase the measured brightness of the Cepheids and lead to a shorter distance. We recall that Bresolin et al. (2005) have tested the effects of crowding for the case of NGC 300 by comparing V- and I-band HST photometry with the ground-based observations and found only a small systematic effect of 0.04 mag. However, in the case of NGC 55 with a surface brightness a magnitude higher the systematic effect might be significantly larger. On the other hand, blue supergiants are several magnitudes brighter than Cepheids and, thus, much less affected by blending. However, even for the supergiants we detect large differences between HST and ground based photometry in the case of NGC 55. We note that the TRGB distance to NGC 55 is 26.62 ± 0.1 mag (EDD database, http://edd.ifa.hawaii.edu, see Tully et al. 2009). The planetary nebulae luminosity function (PLNF) distance modulus by van de Steene et al. (2006) is 26.8 mag, albeit with a relatively large error of ± 0.3 mag. Should our FGLR distances be correct, then NGC 55 would be at a slightly larger distance than NGC 300, 2.34 Mpc versus 1.85 Mpc. With an angular separation of eight degrees (Westmeier et al. 2013) the physical separation would increase from 270 kpc (with the two galaxies at the same distance) to 570 kpc.

At this point, the reasons for the discrepancy between the FGLR and Cepheid distances remain unresolved. A larger sample of blue supergiants with HST photometry and a measurement of HST magnitudes for the Cepheids will be crucial for investigating this issue further.

6. CONCLUSIONS

The comprehensive spectroscopic study of blue supergiant stars distributed over the disk of NGC 55 has led to the first detection of a metallicity gradient in this almost edge on late-type spiral galaxy. The application of a chemical evolution model indicates the effects of intensive infall and outflow, in agreement with recent radio observations of the galaxy, which conclude that the disk is very likely stirred up and disturbed by infalling and outflowing gas. We also find indications of chemical inhomogeneities, which support this picture. The significant difference between the central metallicity of the disk and the metallicity of two extra-planar HII regions above the central disk provides strong evidence for in-situ star formation outside the galactic plane. A distance determination using the FGLR method

leads to a distance which is larger than the distance to the Sculptor group neighbor galaxy NGC 300. Further HST photometry will be needed to settle the issue of distance determination to this galaxy.

The authors wish to express their thanks to the referee whose critical and constructive remarks helped to improve the paper. RPK and FB acknowledge support by the National Science Foundation under grants AST-1008789 and AST-1108906. RPK, MAU, WG were supported by the Munich Institute for Astro- and Particle Physics (MIAPP) of the DFG cluster of excellence "Origin and Structure of the Universe". WG and GP gratefully acknowledge financial support for this work received from the BASAL Centro de Astrofísica y Tecnologías Afines (CATA), PFB-06/2007. WG also acknowledges support from the Millenium Institute of Astrophysics (MAS) of the Iniciativa Científica Milenio del Ministerio de Economía, Fomento y Turismo de Chile, grant IC120009. In addition, support from the Ideas Plus grant of the Polish Ministry of Science and Higher Education and TEAM subsidies of the Foundation for Polish Science (FNP) is acknowledged by GP.

Facilities: VLT:FORS2, HST:ACS

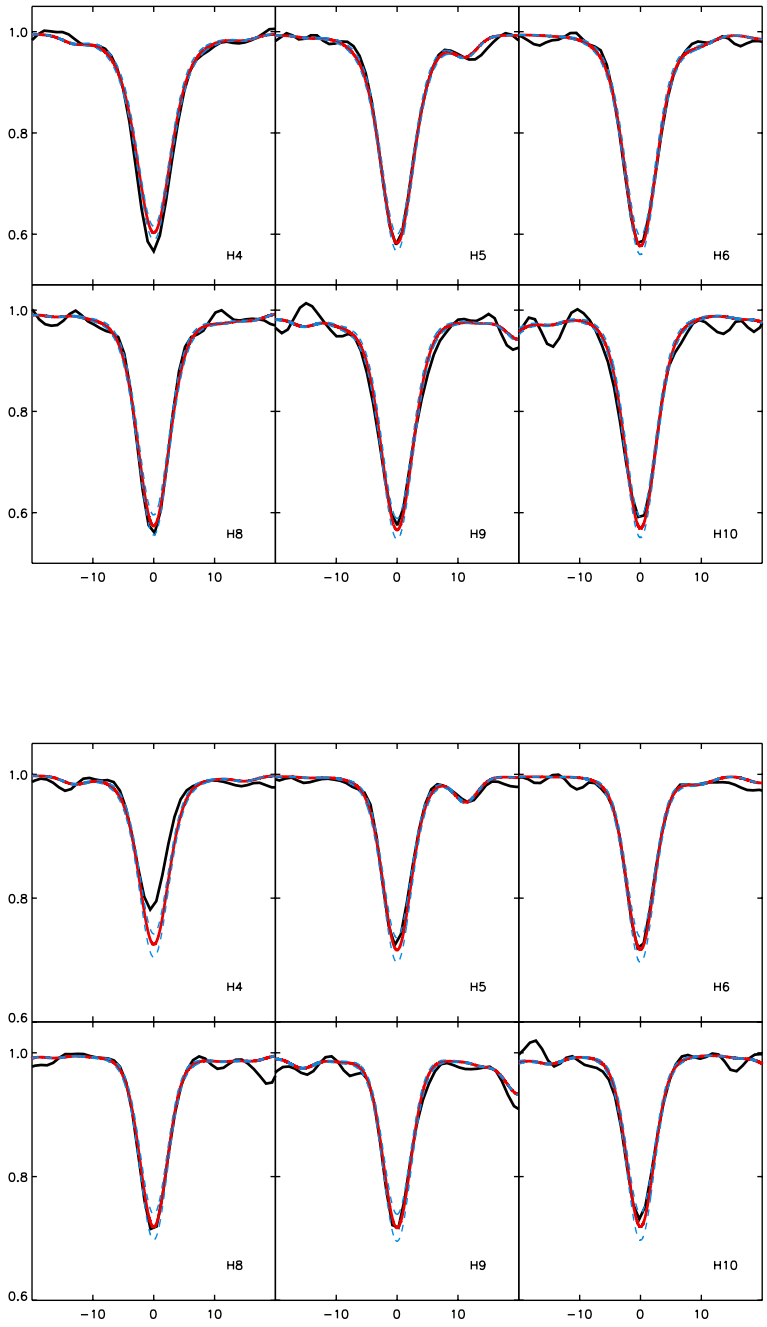

Figure 1. Example model fits of the observed Balmer line profiles for two NGC 55 supergiant stars (black solid). Synthetic profiles of the final model (red) and two models with gravities increased and decreased by 0.05 dex (blue dashed) are overplotted. Top: star C1 49; bottom: star A38.

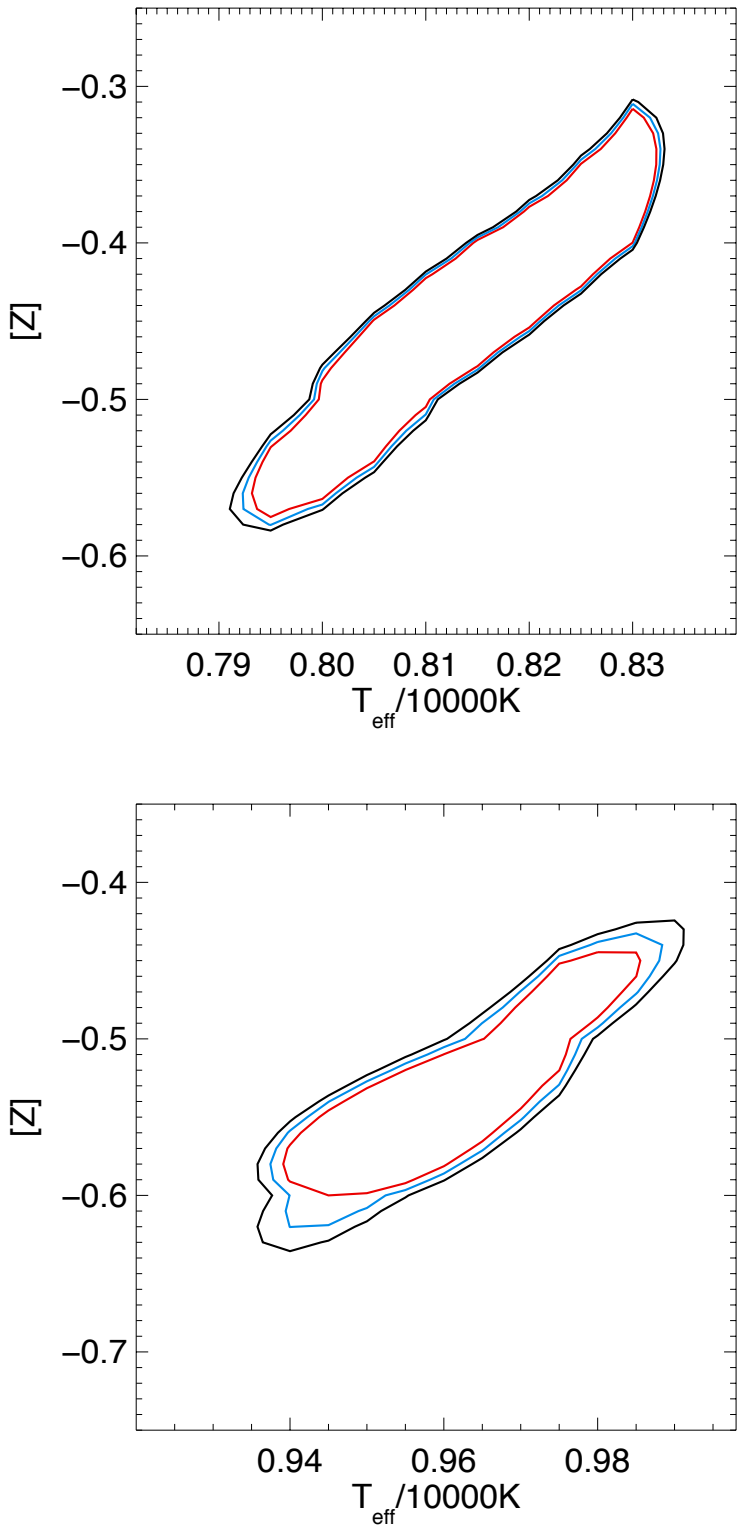

Figure 2. Examples for the determination of effective temperature $T_{\rm eff}$ and metallicity [Z] using isocontours, $\Delta\chi^2$, in the metallicity-temperature plane obtained from the comparison of synthetic with observed spectra (see text). $\Delta\chi^2 = 3$ (red), 6 (blue), and 9 (black), respectively, are plotted. Top: star C1 49; bottom: star A 38.

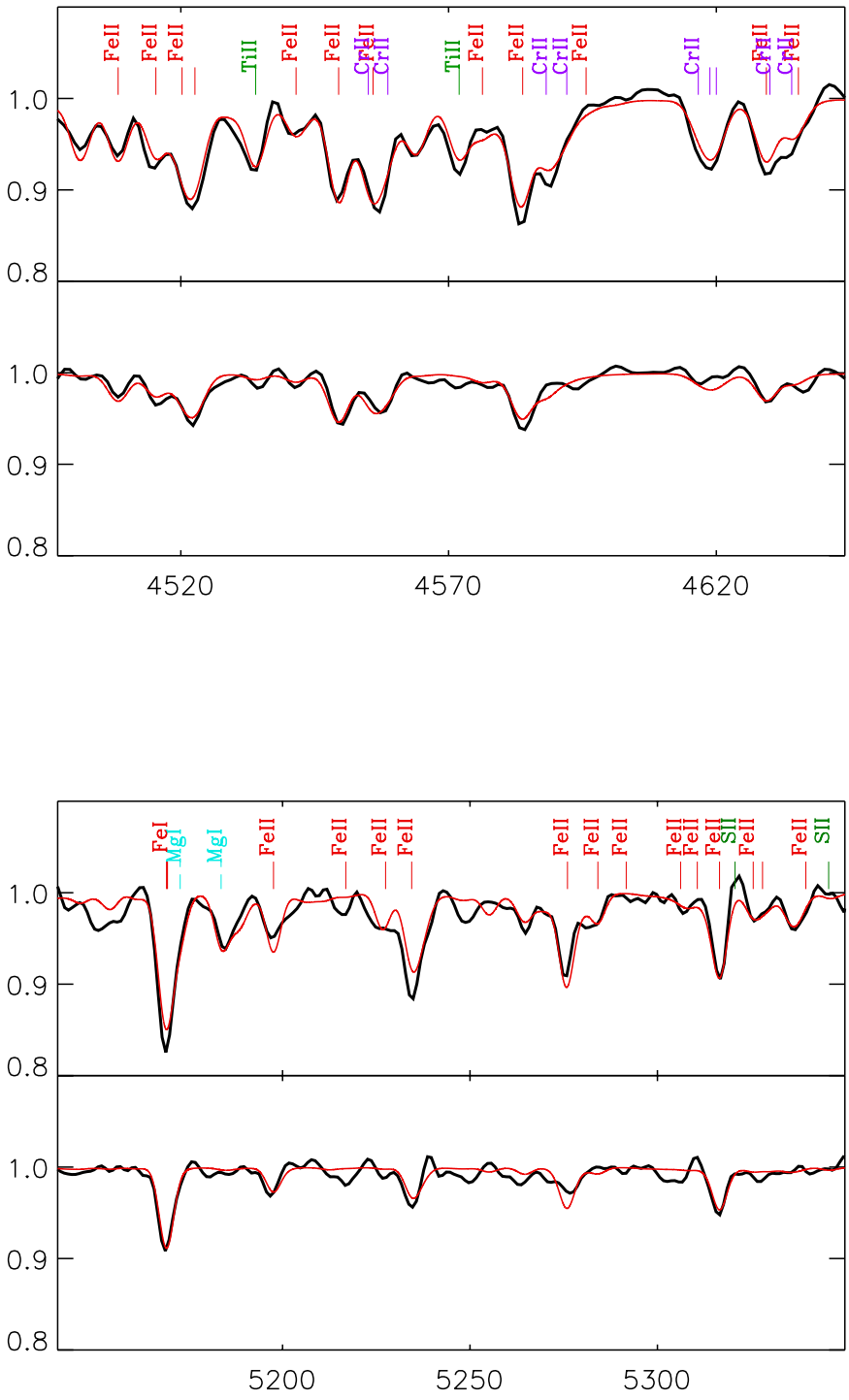

Figure 3. Observed metal line spectra of stars C1 49 (top) and A 38 (bottom) in two spectral windows compared with model calculations (red) obtained for the final stellar parameters of Table 1.

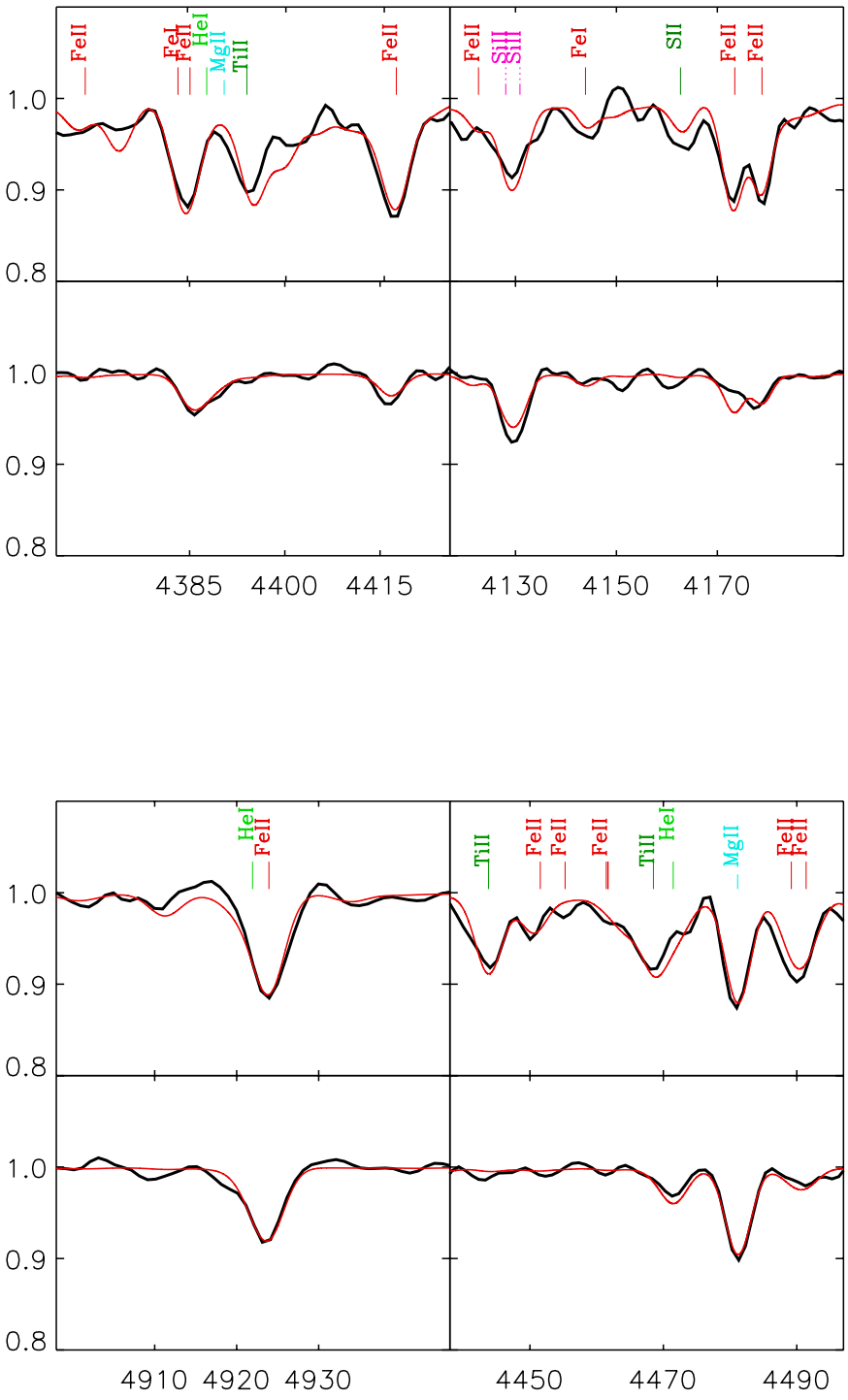

Figure 4. Same as Fig. 3 for four more spectral windows.

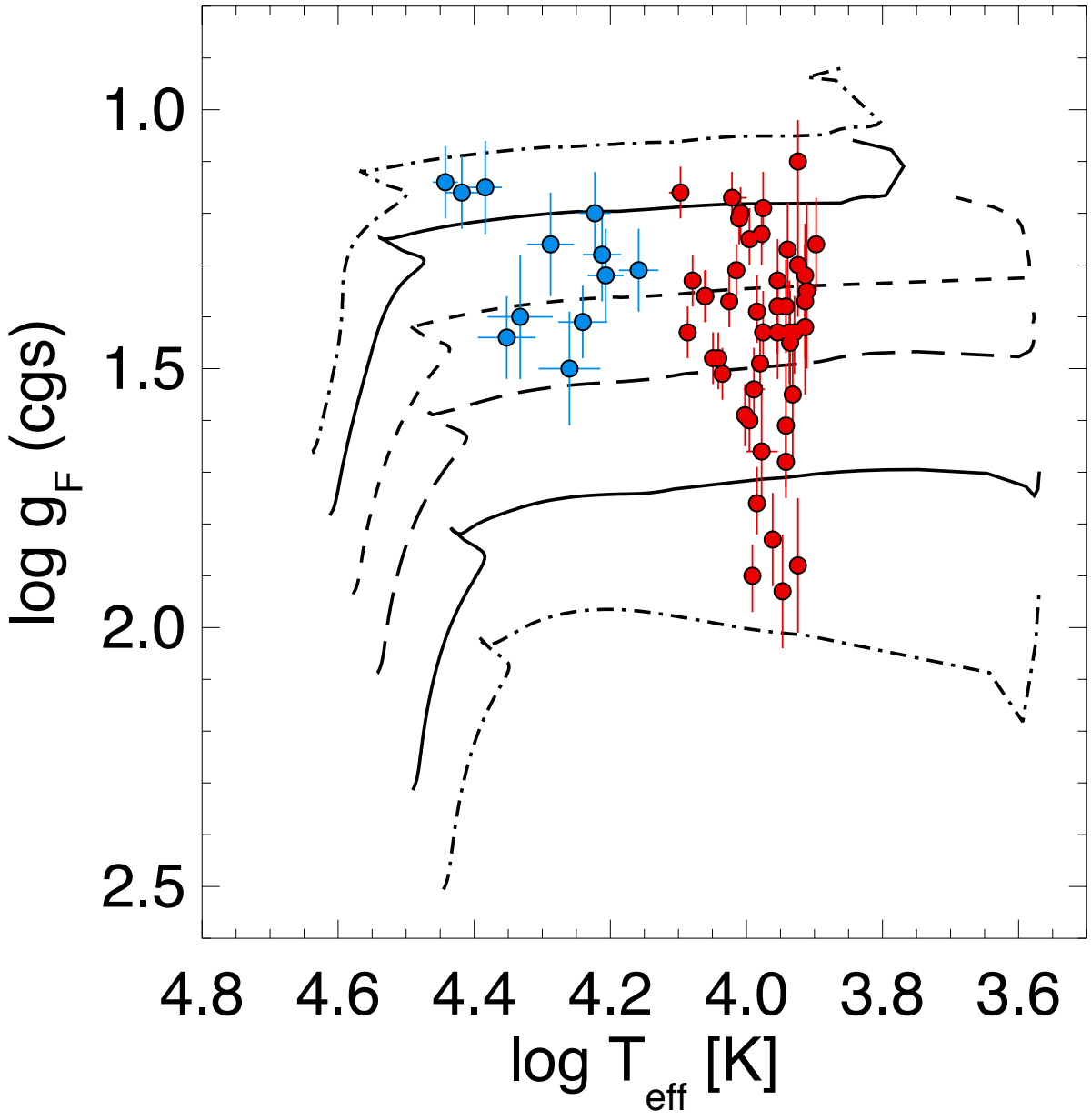

Figure 5. Spectroscopic Hertzsprung-Russell diagram of the NGC 55 supergiant stars of this study compared with evolutionary tracks from Eckström et al. (2012). Blue: early B spectral type, red: late B and early A spectral type. The evolutionary tracks are calculated for initial main sequence masses of (from the bottom of the figure to top) 12, 15, 20, 25, 32 and 40 $M_{\odot}$, respectively, and include the effects of stellar rotation.

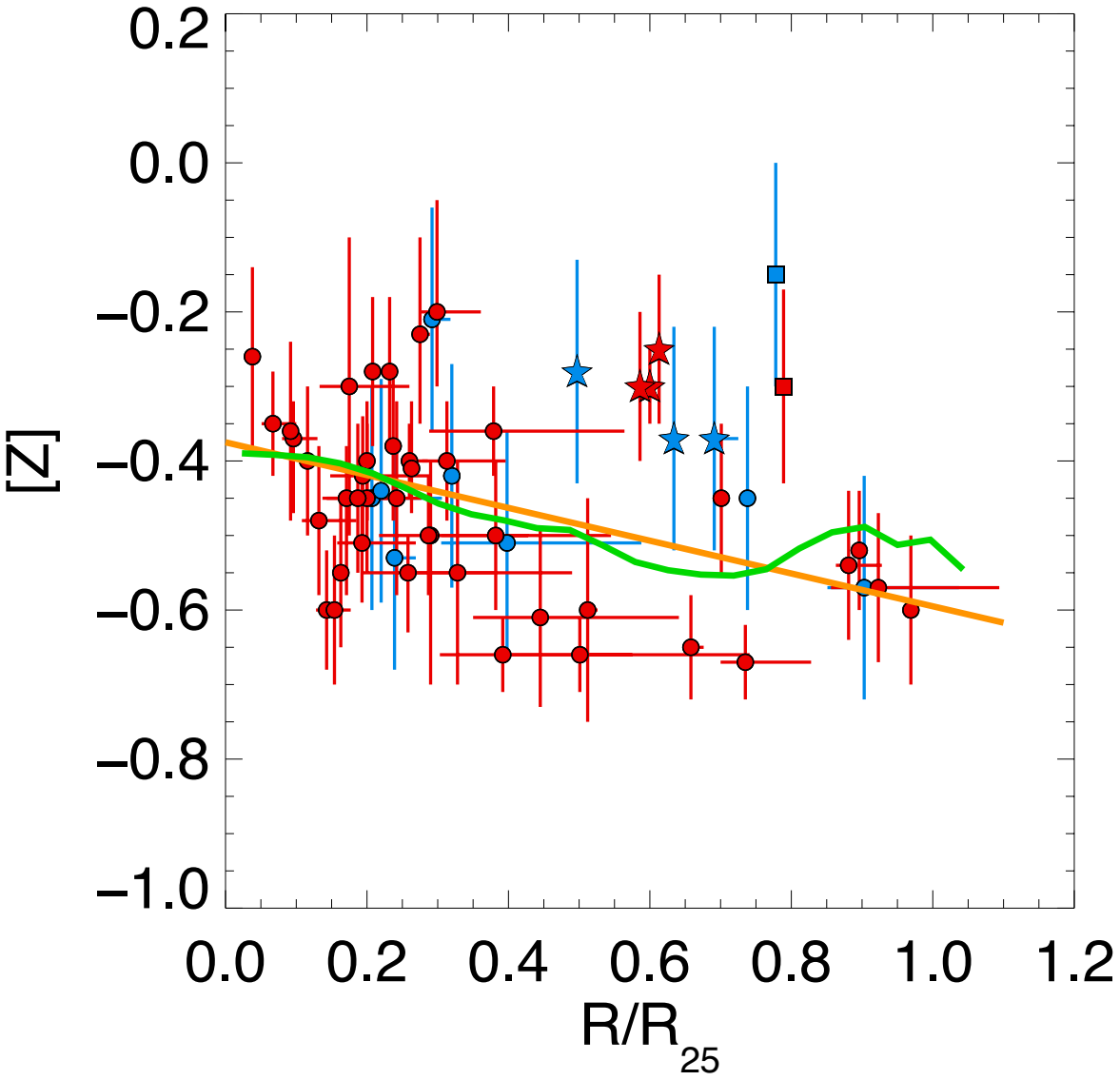

Figure 6. Metallicity of the NGC 55 blue supergiants as a function of galactocentric distance. Blue: early B spectral type, red: late B and early A spectral type. The linear regression accounting for errors in metallicity and galactocentric distance is plotted in orange. Potential outliers are highligthed as squares and stars. The radial metallicity distribution calculated with our chemical evolution model discussed in section 4 is shown in green.

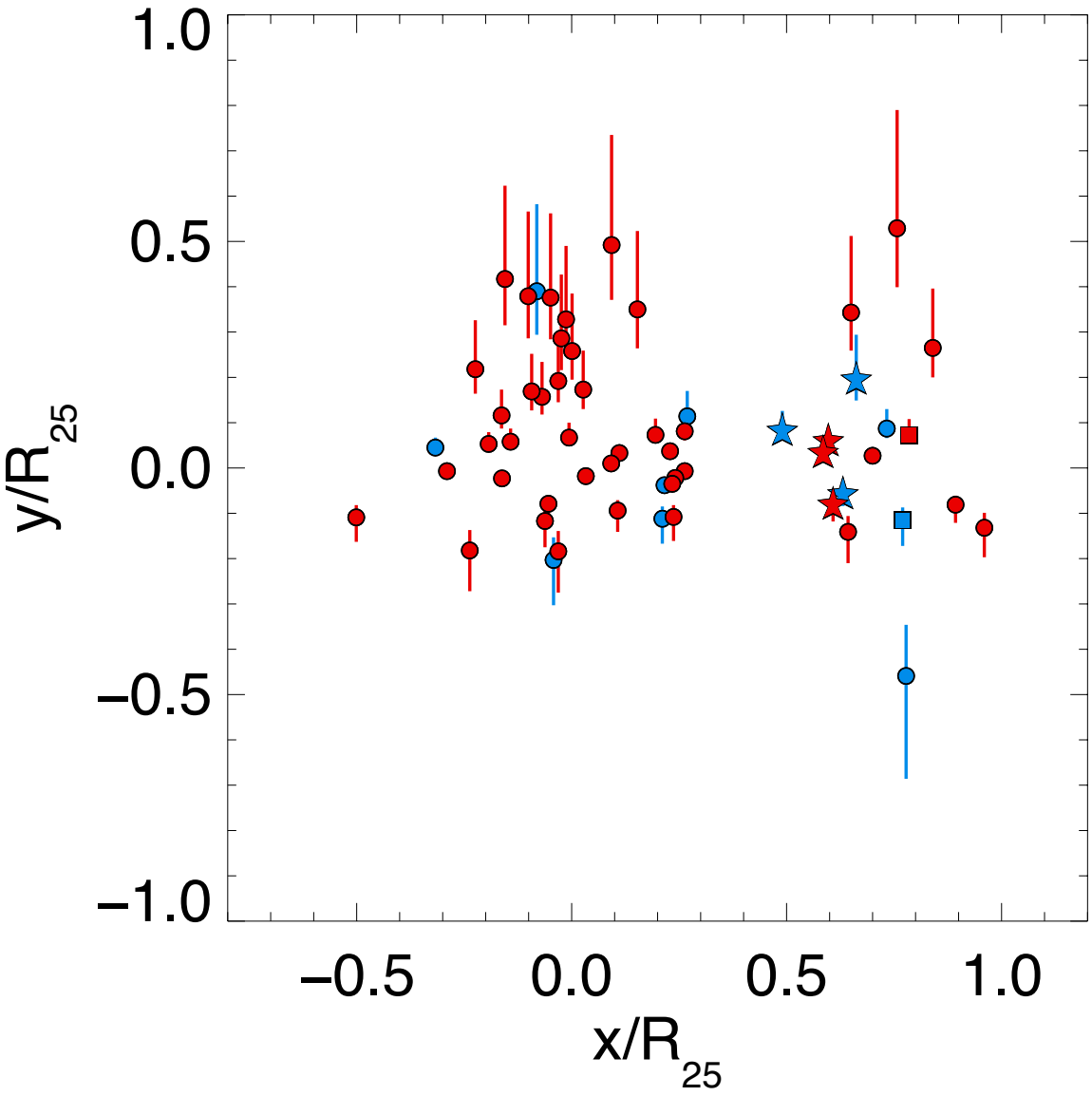

Figure 7. De-projected locations of the NGC 55 blue supergiants in the galactic disk plane. Symbols are the same as in Fig. 6.

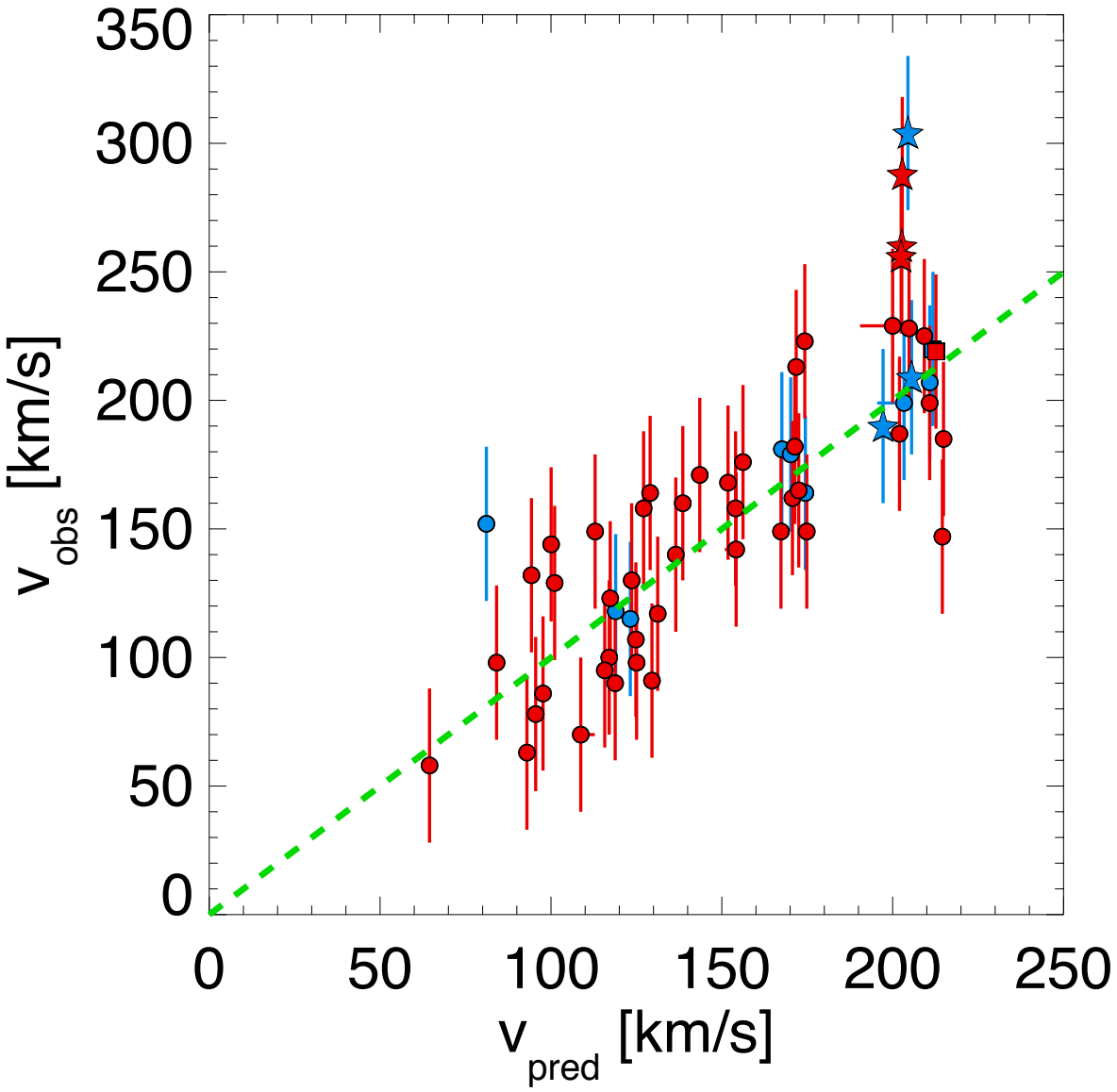

Figure 8. Observed radial velocities of NGC 55 blue supergiants compared with predicted velocities using the rotation curve determined by Puche et al. (1991). Symbols as in Fig. 6. The systemic velocity measured by Westmeier et al. (2013) was adopted (see text).

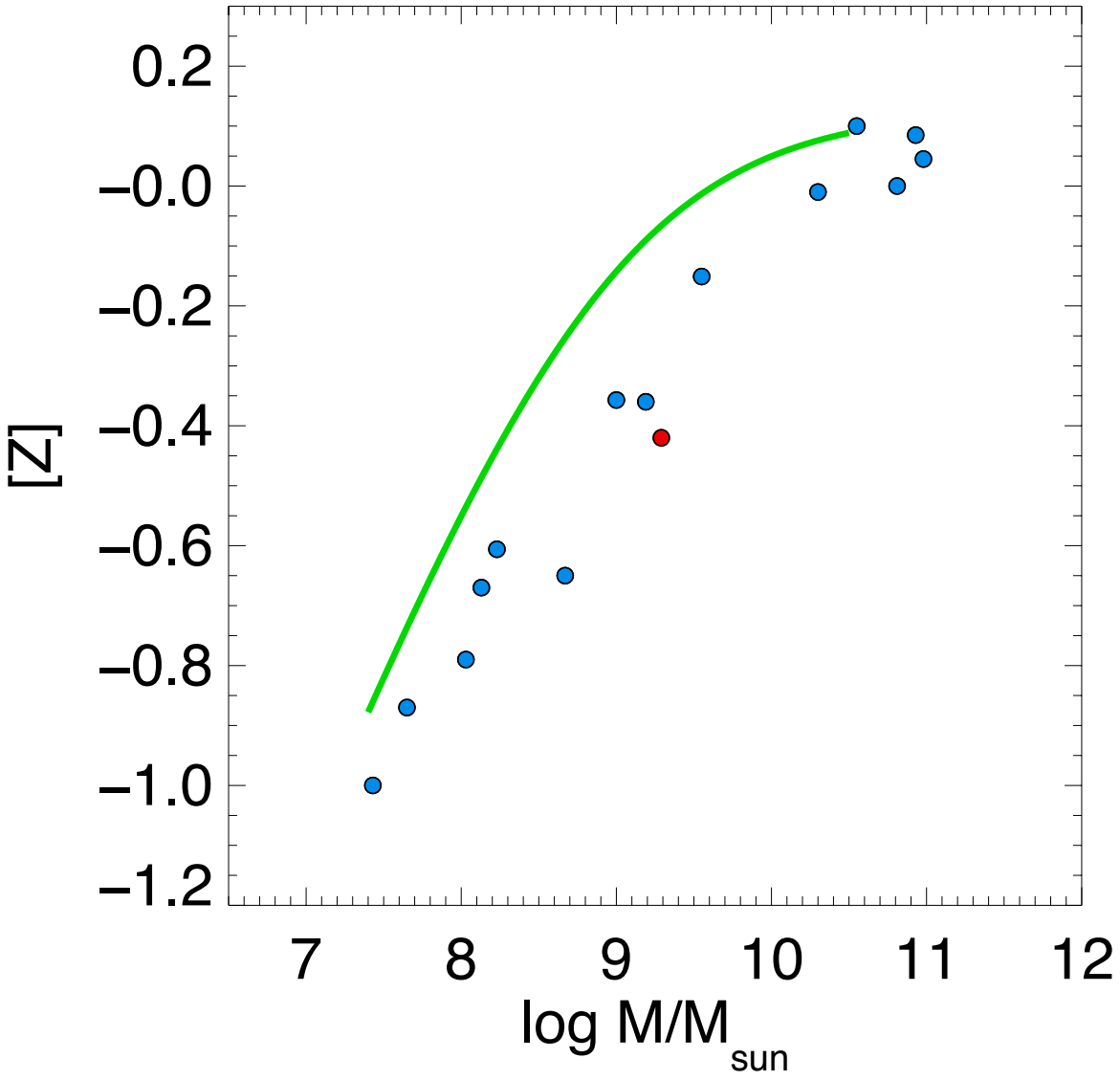

Figure 9. Relationship between total stellar mass and metallicity for a sample of 15 galaxies studied with supergiant spectroscopy (see text). NGC 55 is indicated in red. The green curve is the mass-metallicity relationship obtained by Andrews & Martini (2013) from HII region emission lines of stacked spectra of 50,000 SDSS galaxies using the direct method with auroral lines.

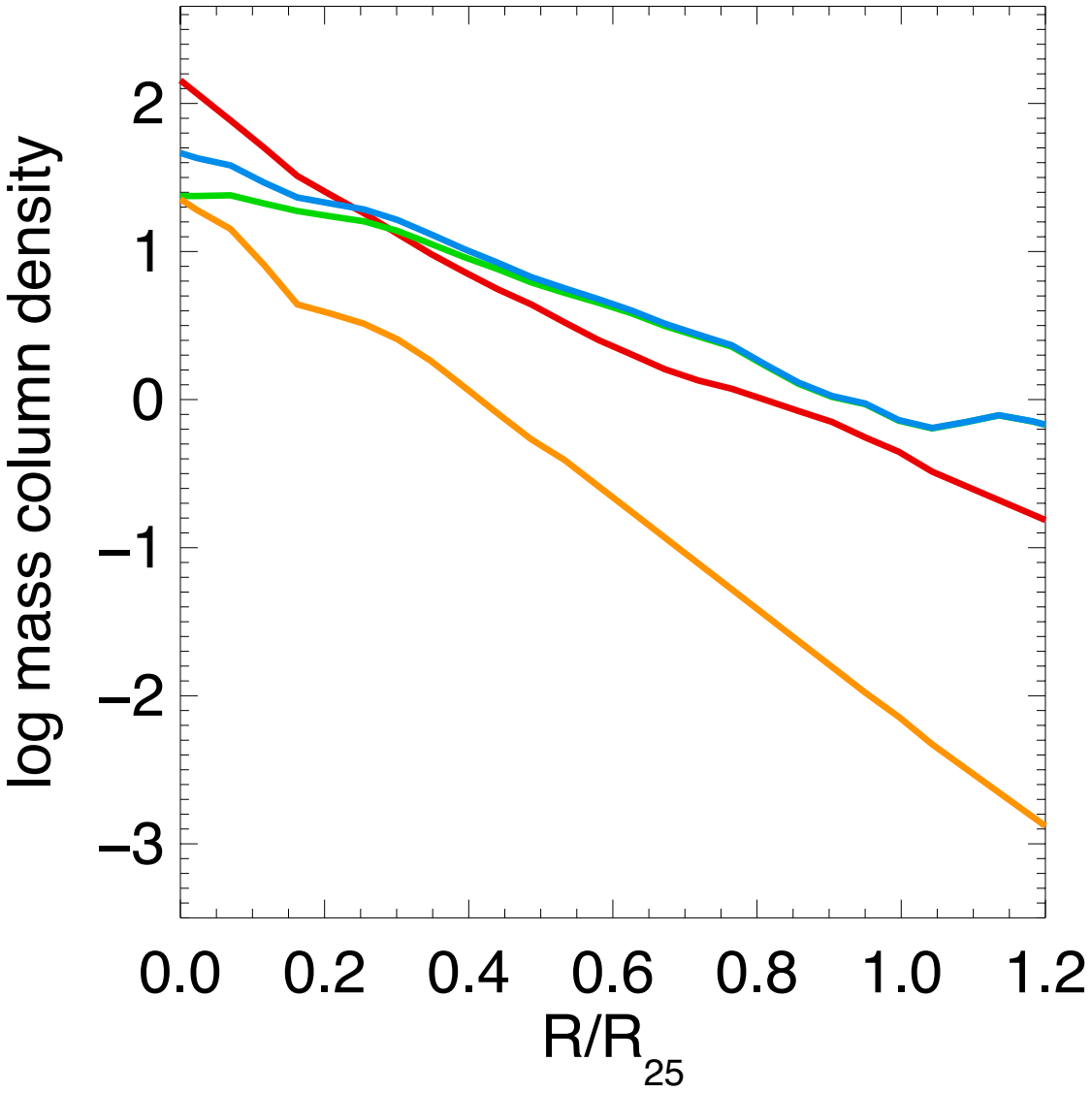

Figure 10. Radial distribution of the logarithm of the de-projected NGC 55 disk mass column densities (in $M_\odot/pc^2$). Red: stellar mass, blue: ISM gas mass, green: atomic gas mass contribution to ISM, orange: molecular gas mass contribution to ISM.

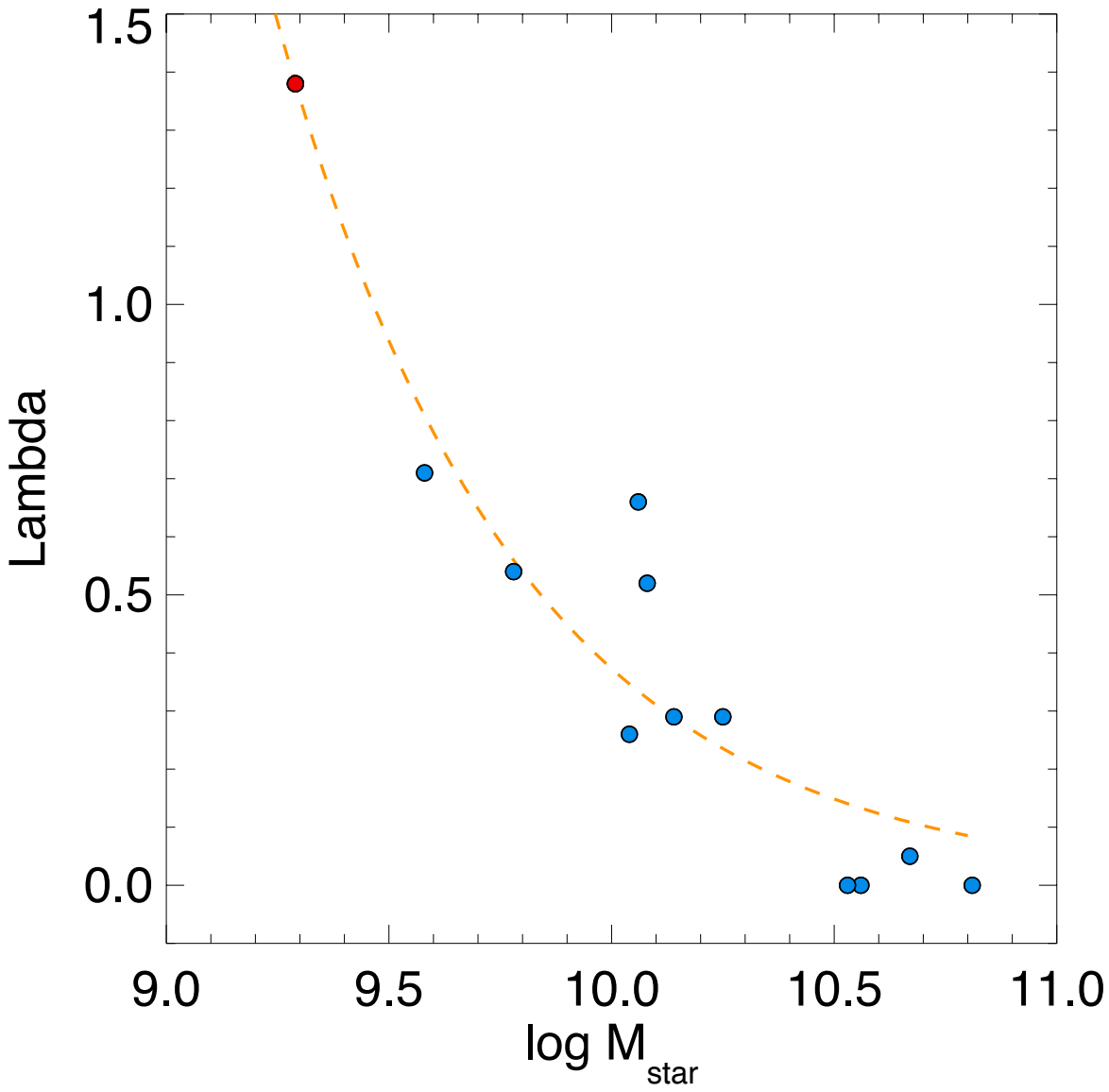

Figure 11. Galaxy mass accretetion rate Λ measured in units of star formation rate as a function of the logarithm of integrated stellar mass (in solar units). Red: NGC 55, blue: galaxies studied by Kudritzki et al. (2015) with well determined values of Λ (see text). The orange dashed curve shows a power law fit $\Lambda \sim M_{star}^{-0.8}$.

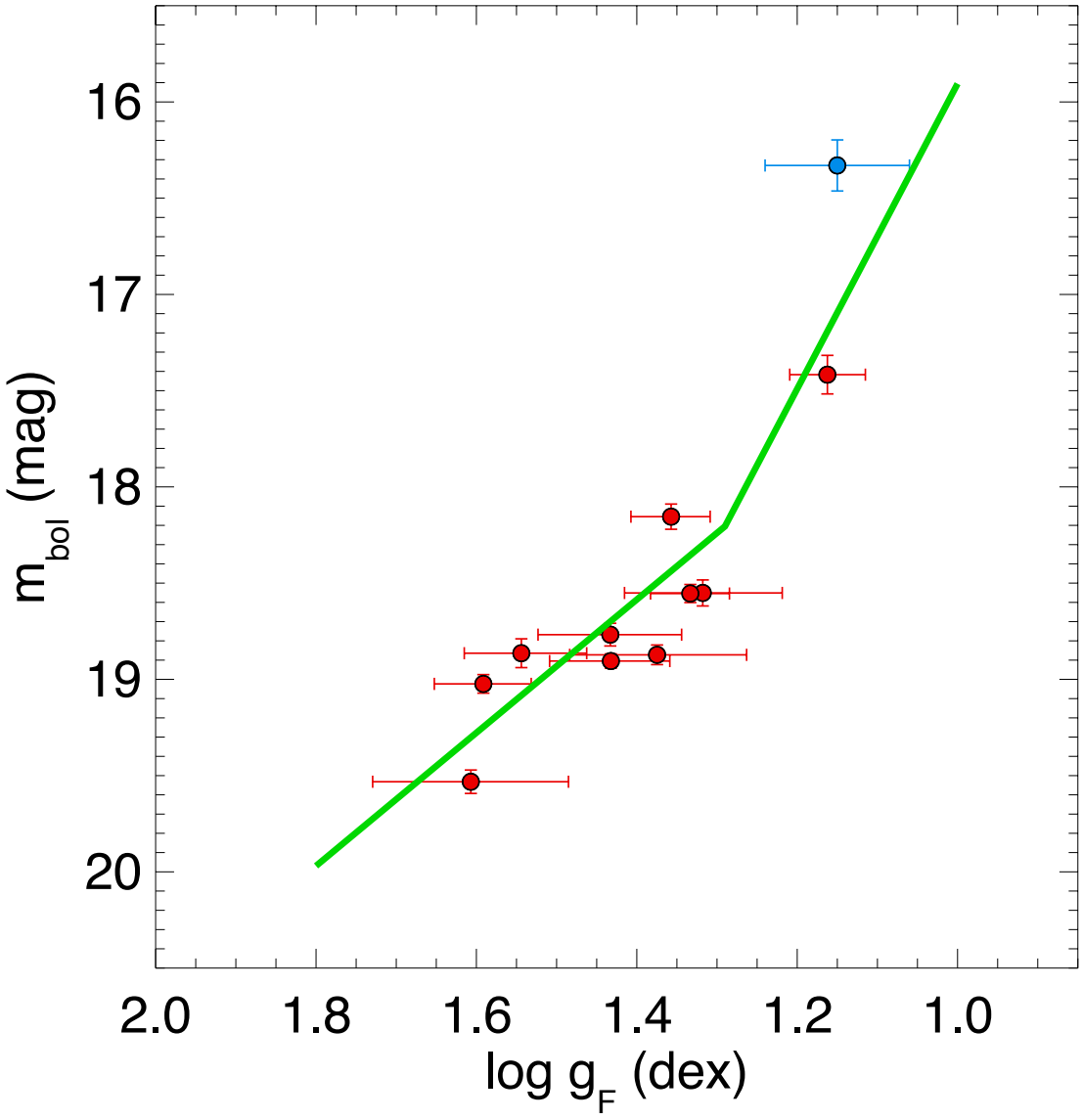

Figure 12. Observed FGLR for the sub-sample of NGC 55 supergiants with HST photometry. The green relation is the LMC FGLR calibration (Urbaneja et al. 2016) shifted to the distance modulus of $m - M = 26.80$ mag. Two targets of Table 4 are not included in the plot because of photometric variability (see text).

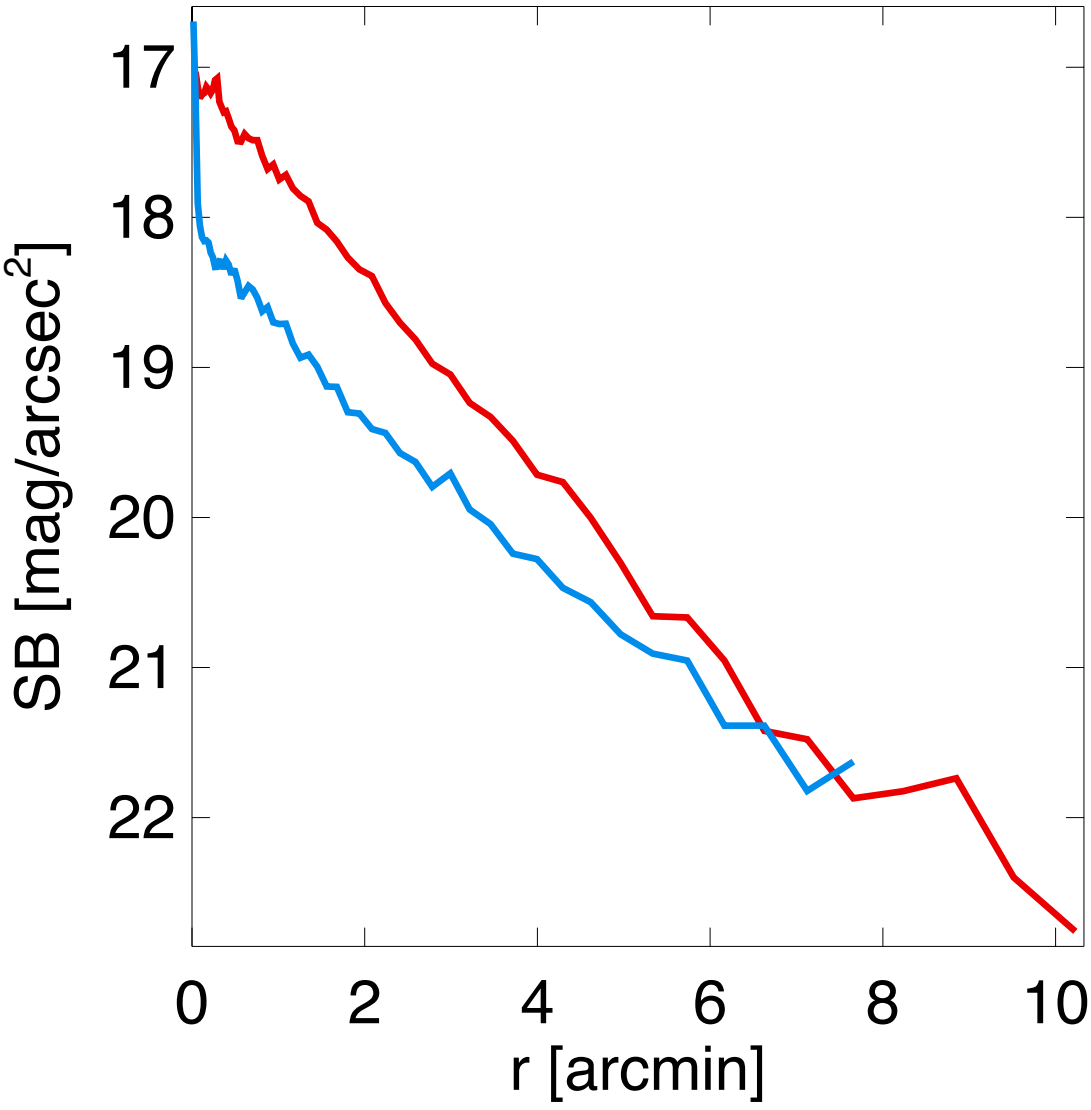

Figure 13. K-band radial surface brightness distribution of NGC 55 (red) and and NGC 300 (blue). Data from the 2MASS website (irsa.ipac.caltech.edu/applications/2MASS/LGA/).

REFERENCES

Andrews, B. H., Martini, P. 2013, ApJ, 765, 140
Asplund, M., Grevesse, N., Sauval, A. J., & Scott, P. 2009, ARA&A, 47, 481
Bresolin, F., Pietrzyński, G., Gieren, W. et al. 2004, ApJ, 600, 182
Bresolin, F., Pietrzyński, G., Gieren, W. et al. 2005, ApJ, 634, 1020
Bresolin, F., Gieren, W., Kudritzki, R. P. et al. 2009, ApJ, 700, 309
Castro, N., Herrero, A., Garcia, M. et al. 2008, A&A, 485, 41
Castro, N., Urbaneja, M. A., Herrero, A.,net al. 2012, A&A, 542, A79
Cutri, R. M., Skrutskie, M. F., van Dyk, S., et al. 2003, VizieR Online Data Catalog, 2246, 0
Dalcanton, J. J., Williams, B. F., Seth, A. C. det al. 2009, ApJS, 186, 67
Dale, D. A., Cohen, S. A., Johnson., L. C. et al. 2009, ApJ, 705, 514
de Vaucouleurs, G. 1961, ApJ, 133, 405
de Vaucouleurs, G., et al. 1991, Third Reference Catalogue of Bright galaxies, Volume I to III
Eckström, S., Georgy, C., Eggenberger, P., et al. 2012, A&A, 537, A146
Evans, C. J. & Howarth, I. D. 2003, MNRAS, 345, 1223
Firnstein, M., & Przybilla, N. 2012, A&A, 543, AA80
Gazak, J. Z., Kudritzki, R. P., Davies, B. et al. 2015, ApJ, 805, 182
Gieren, W., et al. 2005a, ESO Messenger, 121, 23
Gieren, W., Pietrzyński, G., Soscynski, L. et al. 2005b, ApJ, 628, 695
Gieren, W., Pietrzyński, G., Soscynski, L. et al. 2008, ApJ, 672, 266
Ho, I.-T., Wang, W.-H., Morrison, G. E., Miller, N. A. 2010, ApJ, 722, 1051
Hosek, M. W., Jr., Kudritzki, R.-P., Bresolin, F., et al. 2014, ApJ, 785, 151
Hummel, E., Dettmar, R. J., & Wielebinski, R. 1986, A&A, 166, 97
Humphreys, R. M., 1988, in The Extragalactic Distance Scale, ed. S. van den Bergh & C. J. Pritchet (Provo: Brigham Young Univ. Press), 103
Jarrett, D. H., Chester, T., Cutri, R. 2003, AJ, 125, 525
Jerjen, H., Freeman, K. C., & Binggeli, B. 1998, AJ, 116, 2873
Kang, X., Zhang, F., Chang, R., et al. 2016, A&A, 585, 20
Karachentsev, I. D., Grebel, E. K, Sharina, M. E. et al. 2003, A&A, 404, 93
Kewley, L. J., & Ellison, S. L. 2008, ApJ, 681, 1183
Kudritzki, R. P., & Puls, J. 2000, ARA&A, 38, 613
Kudritzki, R. P., Bresolin, F., & Przybilla, N. 2003, ApJL, 582, L83
Kudritzki, R. P., Urbaneja, M. A., Bresolin, F., et al. 2008, ApJ, 681, 269
Kudritzki, R. P., Urbaneja, M. A., Gazak, Z., et al. 2012, ApJ, 747, 15
Kudritzki, R. P., Urbaneja, M. A., Gazak, Z., et al. 2013, ApJ, 779, L20
Kudritzki, R. P., Urbaneja, M. A., Bresolin, F., Hosek, M. W., Jr., & Przybilla, N. 2014, ApJ, 788, 56
Kudritzki, R. P., Ho, I.-T., Schruba, A., et al. 2015, MNRAS, 450, 342
Langer, N., Kudritzki, R. P. 2014, A&A, 564, A52
Lee, N., Sanders, D. B., Casey, C. M., et al. 2015, ApJ, 801, 80
Leroy, A. K, Walter, F., Sandstrom, et al. 2013, ApJ, 146, 19
McGaugh, S. S. 1991, ApJ, 380, 140
Meynet, G., Kudritzki, R.-P., & Georgy, C. 2015, A&A, 581, A36
Pietrzyński, G., Gieren, W., Soszyński et al. 2006, AJ, 132, 2556
Pilyugin, L. S, Grebel, E. K., Kniazev, A. Y. 2014, AJ, 147, 132
Przybilla, N., Butler, K., Becker, S. R., & Kudritzki, R. P. 2006, A&A, 445, 1099
Puche, D., Carignan, C., Wainscoat, R. J. 1991, AJ, 101, 447
Robinson, B. J., van Damme, K. J. 1964, IAU Symposium Vol. 20, p. 287
Stasinska, G., Comte, G., & Vigroux, L. 1986, A&A, 154, 352
Stasinska, G., Pena, M., Bresolin, F., & Tsamis, Y. G. 2013, A&A, 552, 12
Toribio San Cpriano, L., Garcia-Rojas, J., Esteban, C. et al. 2016, MNRAS, 458, 1866
Tüllmann, R., Rosa, M. R., Elwert, T. et al. 2003, A&A, 412, 69
Tremonti, C. A., Heckman, T. M., Kauffmann, G., et al. 2004, ApJ, 613, 898
Tully, R. B., Rizzi, L., Shaya, E. J. et al. 2009, AJ, 138, 323
U, V., Urbaneja, M. A., Kudritzki, R.-P., Jacobs, B. A., Bresolin, F., $ Przybilla, N. 2009, ApJ, 704, 1120
Urbaneja, M. A., Herrero, A., Bresolin, F., et al. 2003, ApJL, 584, L73
Urbaneja, M. A., Herrero, A., Kudritzki, R.-P., et al. 2005, ApJ, 635, 311
Urbaneja, M. A., Kudritzki, R.-P., Bresolin, F., et al., 2008, ApJ, 684, 118
Urbaneja, M. A., Herrero, A., Lennon, D. J., Corral, L. J., & Meynet, G. 2011, ApJ, 735, 39
Urbaneja, M. A., Kudritzki, R. P., Gieren, W. et al. 2016, ApJ, submitted
van de Steene, G. C., Jacoby, G. H., Praet, C. et al. 2006, A&A, 455, 891
Vlajić, M., Bland-Hawthorn, J. & Freeman, K.C. 2009, ApJ, 697, 361
Webster, B. L., Smith, M. G. 1983, MNRAS, 204, 743
Westmeier, T., Braun, R., Koribalski, B. S. 2011, MNRAS, 410, 2217
Westmeier, T., Koribalski, B. S., Braun, R. 2013, MNRAS, 434, 3511
Zahid, H. J., Dima, G. I., Kudritzki, R. P. et al. 2014, ApJ, 791, 130
Zaritzky, d., Kennicutt, R. C., & Huchra, J. P. 1994, ApJ, 420,87